*J. Fluid Mech.* (2023), *vol*. 964, A36, doi:10.1017/jfm.2023.392

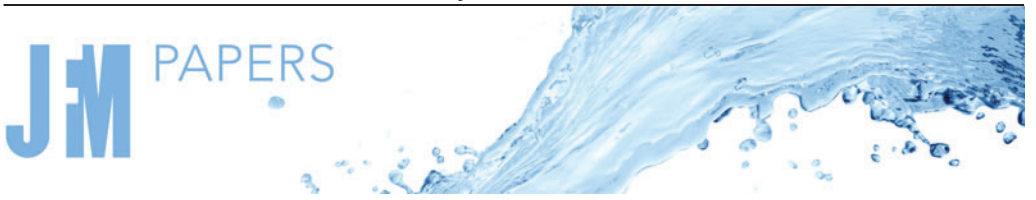

# Experimental investigation of turbulent counter-rotating Taylor–Couette flows for radius ratio $\eta = 0.1$

**Mohammed Hussein Hamede**[1],†, **Sebastian Merbold**[1] **and Christoph Egbers**[1]

[1]Department of Aerodynamics and Fluid Mechanics, Brandenburg University of Technology Cottbus-Senftenberg, Siemens-Halske-Ring 15a, 03046 Cottbus, Germany

(Received 4 November 2022; revised 25 March 2023; accepted 21 April 2023)

Turbulent Taylor–Couette flow between two concentric independently rotating cylinders with a radius ratio of $\eta = 0.1$ is studied experimentally. While the scope is to study the counter-rotating cases between both cylinders, the radial and azimuthal velocity components are recorded at different horizontal planes with high-speed particle image velocimetry. The parametric study considered a set of different shear Reynolds numbers in the range of $20\,000 \leq Re_s \leq 1.31 \times 10^5$, with different rotation ratios of $-0.06 \leq \mu \leq +0.008$. The observed flow fields had a clear dependence on the rotation ratio, where flow patterns evolved with a more pronounced axial dependence. The angular momentum transport is computed as a result of the recorded flow fields and given by a quasi-Nusselt number. The dependence of the Nusselt number on the different rotation ratios shows a maximum for the low counter-rotating case and $\mu_{max}$ is found between $-0.011 < \mu_{max} < -0.0077$. The Nusselt number decreases for stronger counter-rotation until a minimum is reached, where it tends to increase again for higher counter-rotation rates. The space–time behaviour of the turbulent flow showed the existence of patterns propagating from the inner region towards the outer region for all studied counter-rotating cases. In addition, patterns have been found that tend to propagate from the outer region towards the inner region with a novel character at high counter-rotation cases. These patterns enhance the angular momentum transport where a second maximum in the transport mechanism has to be expected.

**Key words:** Taylor–Couette flow, rotating turbulence

† Email address for correspondence: hamede@b-tu.de

## 1. Introduction

For more than a century, the flow in the gap between two independently rotating coaxial cylinders has been studied. The so-called Taylor–Couette (TC) flow is used as one of the paradigmatic systems of the physics of fluids. Its simple and mathematically well-defined geometry, natural periodicity and confinement of fluid volume lead to excellent conditions for experimental and numerical studies. Various concepts and topics in fluid mechanics have been studied by this system. The huge variety of flow states in this system provides the possibility to study the flow in its different phases (laminar and turbulent) and the transition between these two phases (Taylor 1923; Chandrasekhar 1961; Dong & Zheng 2011; VanGils *et al.* 2012). The different hydrodynamic instabilities that occur in the flow lead to the appearance of different patterns (Andereck, Liu & Swinney 1986; Razzak, Khoo & Lua 2019; Merbold *et al.* 2023). The most famous example of the pattern formations in the flow is the centrifugally driven Taylor vortices (TV), which arise in both laminar and turbulent flows (Taylor 1923; Froitzheim *et al.* 2019*a*; Huisman *et al.* 2014; Grossmann, Lohse & Sun 2016). The changing of the driving parameters leads to a series of flow transitions, these flow transitions can be classified into different flows, like circular Couette flow, Taylor vortex flow, periodic non-axisymmetric flow, wavy vortex flow, modulated wavy vortex flow and many others; see Taylor (1923), Synge (1938), Coles (1965) and Lim, Chew & Xiao (1998).

The flow in the gap is mainly controlled by the rotation rate and the geometrical parameters. The main geometrical parameter of the system varies depending on the dimensions of both cylinders, and it is defined by the radius ratio $\eta = r_1/r_2$, the gap width $d = r_2 - r_1$ and the aspect ratio $\Gamma = L/d$, with $r_1$ the inner cylinder radius, $r_2$ outer cylinder radius and $L$ the apparatus length. The flow states in this system are mainly determined by the dimensionless Reynolds numbers $Re_1 = r_1\omega_1 d/\nu$ and $Re_2 = r_2\omega_2 d/\nu$ of the inner and outer cylinders, respectively, with $\nu$ being the kinematic viscosity of the fluid. In this study, in order to measure the shear between the cylinders, the shear Reynolds number introduced by Dubrulle *et al.* (2005) is used,

$$Re_s = \frac{2}{1+\eta}|\eta Re_2 - Re_1| = \frac{2r_1r_2d}{(r_1+r_2)\nu}|\omega_2 - \omega_1|. \tag{1.1}$$

After defining the main flow parameters $Re_1$ and $Re_2$, the flow inside the gap takes its shape. The global system response can be quantified by the angular momentum transport $J_w$ (Eckardt, Grossmann & Lohse 2007),

$$J^\omega = r^3\left(\langle u_r\omega\rangle_{A(r),t} - \nu\frac{\partial}{\partial_r}\langle\omega\rangle_{A(r),t}\right). \tag{1.2}$$

The brackets $\langle\ \rangle_{A(r),t}$ denote an average over a cylindrical surface and time $t$, $u_r$ and $\omega$ denote the radial and angular velocities, respectively. The angular momentum transport is normalized by its corresponding laminar value $J^\omega_{lam} = 2\nu r_1^2 r_2^2(\omega_1 - \omega_2)/(r_2^2 - r_1^2)$ to define the Nusselt number $Nu_\omega = J^\omega/J^\omega_{lam}$, which is in analogy to the Nusselt number in the Reyleigh–Benard (RB) convection (Grossmann & Lohse 2000; Busse 2012), the flow in a fluid container heated from below and cooled from above, which quantifies the heat flux.

Out of the different geometries used to study the TC flow till now, most of them are focused on the so-called 'narrow gaps' where $\eta > 0.7$, and relatively fewer studies are published on geometries with $\eta < 0.7$, which we name the 'wide gaps' flow. The radius ratio $\eta$ is directly related to the curvature effect, which also plays a very important role

in TC flow. The curvature number $R_c = d/\sqrt{r_1 r_2}$, introduced by Dubrulle *et al.* (2005), measures the influence of curvature in terms of the geometrical mean of both cylinder's radii and the gap width $d$. Considering the curvature is important as it affects strongly the geometry and influences the flow field. One of the examples that can explain the effect of the curvature is the Görtler instability. This instability can disturb the viscous boundary layers of flows over concave surfaces by streamwise-oriented counter-rotating vortices named Görtler vortices, leading the flow through a transition to turbulence (Görtler 1954; Saric 1994). As $\eta$ approaches 1, the curvature effect vanishes and $R_c$ becomes zero, where in this situation the TC flow becomes a rotating plane couette (RPC) flow (Brauckmann, Salewski & Eckhardt 2016). They also showed, for $\eta < 0.9$, that the asymmetry inside the gap increases and shows the difference between the inner gap region and the outer region, and the curvature effect becomes more important. This asymmetry inside the gap increases as $\eta$ decreases.

The angular momentum transport has already studied for narrow gaps (Wendt 1933; Lathrop, Fineberg & Swinney 1992; Lewis & Swinney 1999; Ravelet, Delfos & Westerweel 2010; Paoletti & Lathrop 2011; VanGils *et al.* 2012; Brauckmann & Eckhardt 2013; Huisman *et al.* 2014; Ostilla-Monico *et al.* 2014; Nordsiek *et al.* 2015; Grossmann *et al.* 2016; Froitzheim *et al.* 2019*a*), as well as wide gaps (Wendt 1933; Merbold, Brauckmann & Egbers 2013; Dong 2016; Froitzheim, Merbold & Egbers 2017; Froitzheim *et al.* 2019*b*). The angular momentum transport can either be measured by measuring the torque induced in the inner cylinder directly (Merbold *et al.* 2013; Froitzheim *et al.* 2019*b*) or by measuring the velocity field inside the gap and computing the angular momentum transport using (1.2). Froitzheim *et al.* (2017) showed that PIV can sufficiently resolve $J_\omega$ in comparison to a direct torque measurement. A relation between the driving parameter $Re_s$ and the Nusselt number is assumed using a power law ansatz $Nu_\omega \sim Re_s^{\alpha-1}$. The effective scaling of the momentum transport is then used in most of the studies to distinguish between the two different flow regimes in TC flow, the ultimate and the classical regime. The ultimate flow regime is, in analogy to RB convection, the flow with turbulent bulk and turbulent boundary layers (Busse 2012; Huisman *et al.* 2012), while the classical regime is the flow with turbulent bulk and laminar boundary layers. The exponent $\alpha$ changes with $Re_s$, and this change is linked to the shear inside the boundary layer according to (1.2) (Eckardt *et al.* 2007).

Another phenomenon related to the angular momentum transport is observed in the experiments of the same $Re_s$ with varying rotation ratios $\mu$, finding a maximum of angular momentum transport at a specific rotation ratio. For $\eta = 0.716$, Huisman *et al.* (2014) measured a maximum at $\mu_{max} = -0.36$, while for $\eta = 0.724$, Paoletti & Lathrop (2011) measured $\mu_{max} = -0.33$. For a wider gap $\eta = 0.5$, Merbold *et al.* (2013) shows that the maximum occurs at $\mu_{max} = -0.2 \pm 0.02$ using direct torque measurements. Froitzheim *et al.* (2019*b*) finally measured for $\eta = 0.357$ a maximum at $\mu_{max} = -0.123 \pm 0.03$. Ostilla-Monico *et al.* (2014) further confirmed the values of $\mu_{max}$ numerically by finding $\mu_{max} = -0.22$ for $\eta = 0.5$, $\mu_{max} = -0.33$ for $\eta = 0.716$ and $\mu_{max} = -0.123 \pm 0.03$ for $\eta = 0.357$. They also showed that this maximum is connected to the formation of the turbulent TV, which enhance the angular momentum transport.

Different attempts were made to derive a prediction for the position of $\mu_{max}$. A prediction was made by Brauckmann & Eckhardt (2013), where they linked the location of the torque maximum to the onset of intermittency in the gap, and they came back with the prediction written as $\mu_p(\eta) = -\eta^2([(a(\eta)^2 - 2a(\eta) + 1)\eta + a(\eta)^2 - 1]/[(2a(\eta) - 1)\eta + 1])$, where $a(\eta)$ is a factor that computes the extension of the TV beyond the

theoretical neutral line. The prediction yields $\mu_p(\eta = 0.375) = -0.1159$, $\mu_p(\eta = 0.5) = -0.191$ and $\mu_p(\eta = 0.71) = -0.344$ with very good agreement with the aforementioned findings. For the geometry studied here with $\eta = 0.1$, this predicts a torque maximum at $\mu_p(\eta = 0.1) = -0.0097$.

After the different flow regimes in counter-rotating TC flow in a very wide gap ($\eta = 0.1$) were studied in Merbold *et al.* (2023), the scope of the present work is to study the turbulent statistics, $Nu_\omega$, contributions to $Nu_\omega$, and flow temporal behaviour. In this paper the physical behaviour of the fluid is studied in geometry, which has rarely been investigated up to today. Especially here, the circumferential length of the inner cylinder is smaller than the gap width, which is the case for $\eta < 0.14$. Thus, the curvature effect becomes large, but the influence of the rotating inner cylinder decreases on the other side. Thus, the behaviour of the flow in this gap is expected to be different from the other TC geometries with $\eta > 0.14$ (Eckardt *et al.* 2007). As the kinematics of the system differ a lot between co- and counter-rotating cylinders, the scope of this paper is limited to counter-rotation, while the flow behaviour of a co-rotating flow has not been discussed, although some data has been presented shortly as a comparison. These flow states will be the scope of another study.

## 2. Experimental set-up

The top view TC Cottbus (TvTC) facility is used in the current study. Using this TC apparatus, the gap width is changeable by changing the inner cylinder (van der Veen *et al.* 2016; Froitzheim *et al.* 2017; Merbold *et al.* 2023). In the current study the inner and outer cylinder radii used are $R_1 = 7$ mm and $R_2 = 70 \pm 0.2$ mm, respectively, leading to a radius ratio of $\eta = 0.1$ and a gap width of $d = R_2 - R_1 = 63 \pm 0.2$ mm. The height of both cylinders is $L = 700$ mm, leading to an aspect ratio of $\Gamma = L/d = 11.11$. Each cylinder is connected to a direct current motor via a gear transmission belt, so both cylinders can rotate independently.

In a previous investigation using the same facility studying TC flow with different geometries $\eta = 0.357$ (Froitzheim *et al.* 2019*b*), the angular momentum transport was calculated by measuring the torque induced on the inner cylinder with the use of a torque sensor installed in the driving shaft. Unfortunately, the torque acting on the thin inner cylinder in this investigation is below the threshold for accurate measurement using this procedure ($< 2 \times 10^{-5}$ Nm). A second shaft-to-shaft torque sensor with higher sensitivity (Lorenz DR-3000) was used but did not give reliable results. Thus, the actual torque inside the $\eta = 0.1$ system is not able to be determined by the direct method, as done in the prior investigations.

The flow in the gap between both cylinders is restricted by two end plates fixed to the outer cylinders. Both the outer cylinder and the top end plate are made of acrylic glass, enabling optical access to the flow in the gap. Figure 1 shows the PIV set-up used in this study. A Phantom VEO 640 l (2560 × 1600 pixels) high-speed camera is mounted at the top of the apparatus, and an LDY.300PIV laser ($\lambda = 532$ nm, $P_0 = 15$ mJ) is placed beside the apparatus, the laser output is transported using a guiding arm, which generates a horizontal laser sheet through the gap as shown in the figure 1. The laser sheet's position is adjustable, allowing us to measure the flow velocities at different heights. This PIV set-up allows for measuring the radial ($u_r$) and azimuthal ($u_\phi$) velocity components in the gap at different heights. Distilled water ($\nu(20\,^\circ\mathrm{C}) = 10^{-6}$ m$^2$ s$^{-1}$) is used as a working fluid. The fluid is seeded with silver-coated hollow glass spheres as tracer particles, with a mean

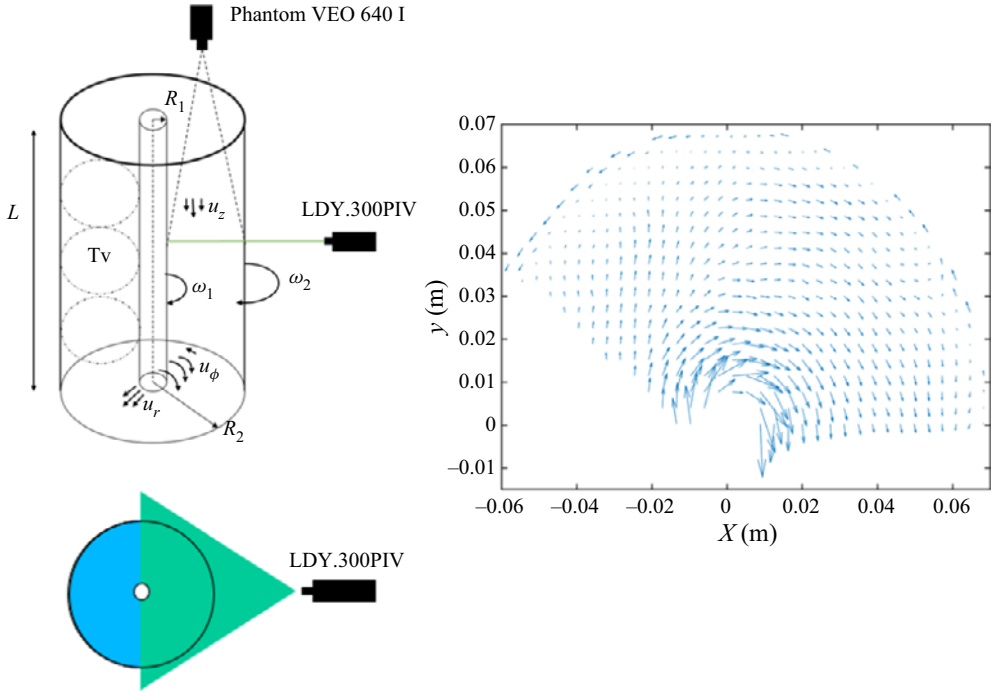


Figure 1. (*a*) Schematic of the TC apparatus with the PIV set-up, and the horizontal cross-section of the set-up with the horizontal laser sheet. (*b*) Mean velocity field in the azimuthal-radial plane at mid-height for $\mu = -0.007$ and $Re_s = 6.1 \times 10^4$ obtained using PIV. Every fourth vector in each row and column is plotted in this representation to improve readability.

diameter of 10 μm, with Stokes number

$$St = \left(\frac{\rho_p}{\rho} - 1\right)\frac{d_p^2 u_s}{18\nu d}, \tag{2.1}$$

assuming a max speed of 2 m s$^{-1}$, $St = 1.7 \times 10^{-4}$, so $St \ll 1$. Furthermore, and considering the flow to be turbulent, the turbulent length scale $\eta_k = (\nu^3/\epsilon)^{1/4}$ is calculated for $Re_s = 1.3 \times 10^5$, where according to Eckardt *et al.* (2007)

$$\epsilon = \frac{2J_\omega \Delta\omega}{(r_2^2 - r_1^1)}. \tag{2.2}$$

As an assumption for the minimum length scale, a high turbulent angular momentum transport of $J_\omega = 100 J_{lam}$ is estimated, with $J^\omega_{lam} = 2\nu r_1^2 r_2^2(\omega_1 - \omega_2)/(r_2^2 - r_1^2)$. Hence, $\eta_k = 6 \times 10^{-5}$ m is larger than the particle's mean diameter, confirming that they follow the flow precisely in all measured cases in this study.

We are aware of the weakness of two-dimensional (2-D) measurements in a three-dimensional (3-D) flow. But a full 3-D measurement would first reduce the spatial resolution significantly (Tokgöz *et al.* 2012), and add uncertainties from camera angle views. In addition, it will add calibration issues while capturing the flow through the cylindrical outer cylinder. For all the previously stated reasons, we choose to scan the volume in the third dimension to understand the axial dependence of the flow by measuring the flow in the horizontal $\phi r$ plane at different heights. By changing the

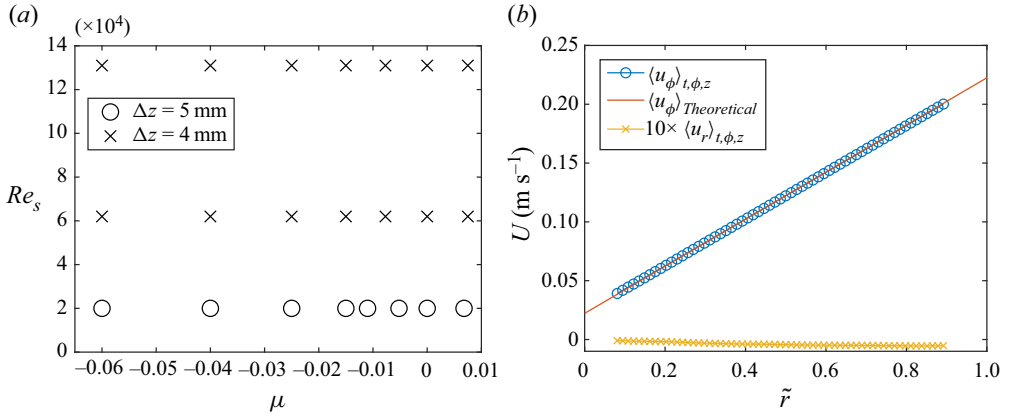


Figure 2. (*a*) The investigated parameter space in terms of $Re_s$ and $\mu$. (*b*) The time and radial averaged profile of the azimuthal and radial velocities compared with the solid body velocity.

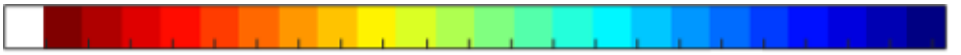


| $\Delta z$ (mm) | 40 | 28 | 16 | 0 | −16 | −28 | −40 |
|---|---|---|---|---|---|---|---|
| Scale factor (m px$^{-1}$) $\times 10^{-5}$ | 7.139 | 7.316 | 7.505 | 7.750 | 7.993 | 8.177 | 8.378 |

Table 1. Scale factor at different heights. The colour map depicts the colours used to represent data at different heights. This representation is used in all sections of the current study.

altitude of the horizontal laser sheet, the flow in the gap at different heights is measured. The measurements are done for heights between 40 mm above and 40 mm below the mid-height for $Re_s = 6.1 \times 10^4$, $1.31 \times 10^5$ and between 40 mm above and 90 mm below for $Re_s = 20\,000$. Figure 2(*a*) shows the parameters investigated in the current study. For the higher shear Reynolds number, the flow is measured at 21 different heights, with a distance of $\Delta z = 4$ mm between each height. While for lower $Re_s$, the measurements are done for 27 heights with $\Delta z = 5$ mm resulting in a longer range in $z$. Enlarging $\Delta z$ is supported by previous flow visualizations, where the axial dependence is observed to be less. The camera is mounted at a fixed height, so by adjusting the height of the laser sheet, the camera lens needs to be refocused to capture the flow at the desired height. Refocusing the camera lens at each height leads to different spatial resolutions for the different heights, as shown in table 1.

For $Re_s = 20\,000$, the measurements are done for 7 s with 200 frames per second, which comes out with 1400 PIV images at each height. For the higher $Re_s$, the measurement time is increased to 10 s to better capture the temporal behaviour of the flow, using the same frame rate, which comes out with 2000 PIV images for each height. The single frame mode is used, as the time between every two consecutive images is $\Delta t = 0.005$ s, which suits the displacement for the velocities of the experiment. Furthermore, the Kolmogorov micro time scale $\tau_K = (\nu/\epsilon)^{1/2}$ for the maximum investigated turbulent case $Re_s = 1.3 \times 10^5$, and by assuming a maximum $J_\omega = 25 J_{lam}$ (cf. figure 8), computes to $\tau_K = 0.00733$. As $\tau_K > \Delta t$, it is ensured that the measured data are time resolved. The PIV images

are post-processed using LaVision Davis software. The velocities are calculated using an adaptive PIV algorithm, with the final interrogation area (IA) being $24 \times 24$ pixels with 50 % overlap. The velocity data are transformed using MATLAB 2019b to a polar coordinate velocity $(u_\phi, u_r)$ and interpolated onto a polar grid of concentric cylinders of fixed radii $r$. After this interpolation, the data matrices at each instantaneous time are reorganized in such a way that all the data belonging to the same radial position are presented in one column, and for the different radial positions, the data has been presented in the same azimuthal domain.

The circumference of the inner cylinder is 10 times smaller than the outer cylinder. Thus, the spatial number of azimuthal samples in the radial position close to the inner cylinder is 10 times less than that for the radial position close to the outer cylinder. This can be a source of uncertainty for any statistical analysis, but the number of temporal samples (2000 images or 1400 images) for each measurement set can compensate for this uncertainty. Another source of uncertainty might be the calibration error. For the calibration, the same procedure used in Froitzheim *et al.* (2017) is used in the current study. For further details about the calibration procedure, the reader is referred to Hamede, Merbold & Egbers (2023).

To verify our measurement accuracy, a measurement set is performed using solid body rotation with $\omega_1 = \omega_2 = 33.5$ rpm over the 21 different heights. Figure 2(*b*) compares the temporally, azimuthally and axially averaged azimuthal and radial velocity profiles of the solid body to the theoretically predicted velocity profiles. The comparison between the measured azimuthal velocity profile and the solid body velocity profile shows a very good agreement, with a maximum error of 1 % in the inner region of the gap and 0.3 % in the outer region. Although in the solid body rotation the radial velocity vanishes, the results of our measurement show a very low value with a maximum of $-0.5$ mm s$^{-1}$ that represents 0.4 % of the mean azimuthal velocity, which is considered low. So, in conclusion, the measured velocities in this case and our entire set of velocity measurements used in this study can be considered to have high accuracy.

During the measurements, the fluid temperature rises up to 2 K, as every measurement set of 21 or 27 heights takes between 1.5 and 2 h to be performed. During the measurements, the inner cylinder is rotating at high speed, which heats up the bearings and causes an increase in the fluid temperature. In order to solve this problem, the fluid temperature inside the gap is continuously measured using a temperature sensor, and for every rise in temperature, the velocity of the rotating cylinders is adjusted so that the dimensionless parameters $(Re_s, \mu)$ are guaranteed to be constant for every single measurement set.

## 3. Flow field features

### 3.1. *Dependence of the flow structures on the rotation ratio*

Different flow parameters control the flow inside the TC apparatus; one of these main parameters is the rotation ratio $\mu = \omega_2/\omega_1$. Concerning the rotation ratio, the flow can be distinguished into three regimes: pure inner cylinder rotation ($\mu = 0$), counter-rotation ($\mu < 0$) and co-rotation ($\mu > 0$). Figure 3 shows the contour plots and velocity profiles for the azimuthally and temporally averaged normalized radial $\widetilde{u_r} = u_r/u_s$ and azimuthal $\widetilde{u_\phi} = (u_\phi - u_{\phi,2})/u_s$ velocities, with

$$u_s = \frac{2}{1+\eta}|\eta u_{\phi,2} - u_{\phi,1}|, \quad u_{\phi,2} = \omega_2 r_2, \; u_{\phi,1} = \omega_1 r_1 \tag{3.1}$$

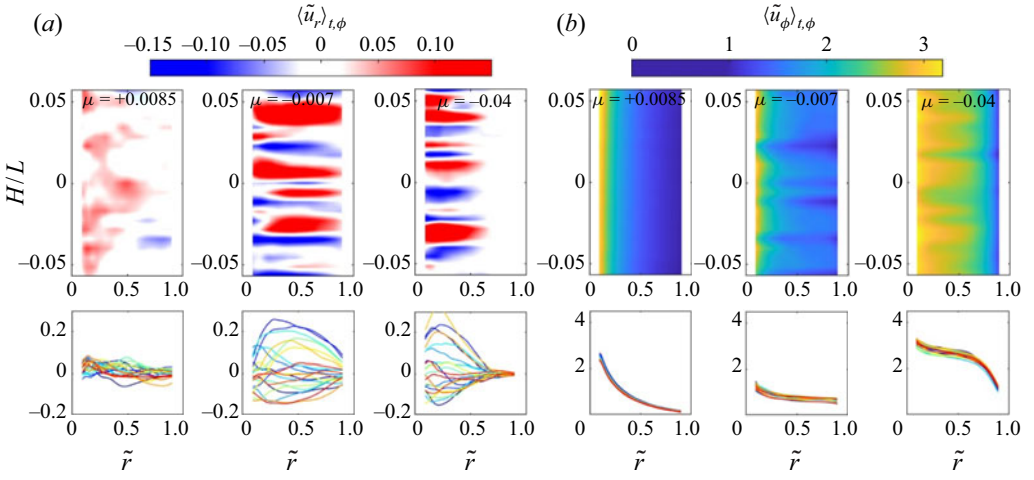


Figure 3. Contour plots and velocity profiles showing the dependence of the normalized temporally and azimuthally, (*a*) radial velocity $\tilde{u}_r$, (*b*) azimuthal velocity $\tilde{u}_\phi$ components. Profiles are plotted for 21 different heights for $Re_s = 6.1 \times 10^4$ and the rotation ratios $\mu = +0.0085, -0.007, -0.04$. Colours represent positions according to table 1.

for a shear Reynolds number $Re_s = 6.1 \times 10^4$ and rotation ratios $\mu = +0.0085, -0.007, -0.04$, for 21 different heights, 10 heights above the apparatus mid-height and 10 below.

The radial coordinate used in the different figures is the dimensionless gap position $\tilde{r} = (r - r_1)/(r_2 - r_1)$, so for $(r = r_1)$, $\tilde{r} = 0$ and, for $(r = r_2)$, $\tilde{r} = 1$. For $\mu = +0.0085$, where the outer cylinder co-rotates with the inner cylinder, the normalized time and azimuthally averaged radial velocity are mostly zero along all heights throughout the gap, with only a very weak outflow near the inner cylinder. On the other hand, the azimuthal velocity component changes noticeably with the radial position, where the velocity profile of the 21 height collapses into one line. Going to the second flow regime, the counter-rotating regime, and starting with the low counter-rotation $\mu = -0.007$, a significant difference compared with the previous case is observed, where the radial velocity shows a clear variation along the different heights, and inflow and outflow regions exist. These inflow and outflow regions can be a fingerprint of a rotating pattern in the gap, like those observed by Froitzheim *et al.* (2017), but in the present case these regions are axially short measured in the radial dimension. The axial wavelength of classical and turbulent TV is usually in the order of $L \approx 2d$ (i.e. for $\eta = 0.5$ in Froitzheim *et al.* 2017), while here we observe an axial wavelength of $L \approx 0.43d$. Thus, the observed flow structures are strongly elliptical, and in contrast to classical vortical patterns, they are better described as interlaced fingers of inflow and outflow. In these inflow and outflow regions, the angular momentum is transported strongly across the gap, as shown in § 4.1. For $\mu = -0.007$, the azimuthal velocity is nearly independent of the height, and like the previous case, the velocity profiles of the 21 height collapse into one line. However, the profiles show a small decrease near the inner cylinder and depict a flat profile with the smallest gradient in the bulk and near the outer cylinder. By increasing further the counter-rotation rate, the angular momentum induced by the outer cylinder stabilizes the flow near the outer cylinder (see figure 3, $\mu = -0.04$). Near the outer cylinder $\tilde{u}_r$ is mostly zero, while close to the inner cylinder it shows the same behaviour as in the $\mu = -0.007$ case. In other words, the axial dependence of the profiles here is restricted to the inner part of the gap, where the magnitude of the radial velocity does not decrease compared with

the $\mu = -0.007$ case. These results show a difference between the very wide gap TC flow studied here and the geometries studied previously, where Froitzheim *et al.* (2017) found, for $\eta = 0.5$, that the magnitude of the radial velocity component decreases significantly when the axial variation of the flow is limited near the inner cylinder. In contrast to the radial velocity, the azimuthal velocity shows a weak axial dependency in the bulk, but it varies near the inner and outer boundaries along the heights. The different flow regimes observed in the currently studied TC geometry are presented and discussed in detail in Merbold *et al.* (2023).

### 3.2. *Averaged velocity profiles*

Given the general overview of the dependence of the flow organization on the rotation rates in the previous section, and to better understand the influence of the rotation ratio $\mu$ and the shear Reynolds number ($Re_s$) on the flow, the temporal and spatial averaged $(t, \phi, z)$ radial profiles of the normalized angular velocity $\tilde{\omega} = (\omega - \omega_2)/(\omega_1 - \omega_2)$ with $\omega = u_\phi/r$, and the normalized angular momentum $\tilde{L} = (L - L_2)/(L_1 - L_2)$ with $L = r^2\omega = u_\phi r$ are analysed, where the angular velocity $\omega$ is the transported quantity in TC flow (see Eckardt *et al.* 2007).

As the scope of our study is to understand the behaviour of the bulk, all profiles are studied for the radial positions in the range of $0.1 < \tilde{r} < 0.9$. The thin boundary layers at the cylinder walls are not well resolved while measuring the flow in the entire gap. The thickness of the boundary layers and the boundaries of the bulk are difficult to define. In particular for very wide gap geometries, a big difference between the thickness of the inner boundary layer ($\lambda_i$) and the outer boundary layer ($\lambda_o$) is expected, as estimated by Eckardt *et al.* (2007), where they derived $\lambda_i/\lambda_o \approx \eta^3$ and, for $\eta = 0.1$, it computes to $10^{-3}$. Also, the different measurements in this study are done for high shear Reynolds numbers, which reduces the size of the boundary layers additionally. For $\eta = 0.5$, Froitzheim *et al.* (2017) assumed that the effect of boundary layers is negligible in the radial positions between $0.1 \leq \tilde{r} \leq 0.9$ and, therefore, assumed this range to be fully dominated by the bulk flow. For the wider gap, even thinner boundary layers are expected, so it can be assumed that both the inner and outer boundary layers are not represented in the limits of $0.1 \leq \tilde{r} \leq 0.9$.

Analysing the dependency of $\omega(r)$ profiles on the driving parameters $Re_s$ and $\mu$ is useful to understand how transport takes place in the flow. The profiles can be compared with the laminar circular Couette solution of the Navier–Stokes equation (for $\eta = 0.1$), which is given by

$$\omega_{lam}(r) = A + \frac{B}{r^2}, \quad L_{lam}(r) = Ar^2 + B, \tag{3.2a,b}$$

$$A = -\omega_1 \frac{\eta^2 - \mu}{1 - \eta^2}, \quad B = \omega_1 r_1^2 \frac{1 - \mu}{1 - \eta^2}. \tag{3.3a,b}$$

The laminar profile is normalized like the measured profiles, so it becomes independent of the cylinder speeds: thus,

$$\tilde{\omega}_{lam}(r) = \frac{1}{1 - \eta^2}\left(\left(\frac{r_1}{r}\right)^2 - \eta^2\right), \tag{3.4}$$

$$\tilde{L}_{lam}(r) = \frac{1}{1 - \eta^2}\left(1 - \left(\frac{r}{r_2}\right)^2\right). \tag{3.5}$$

Finally, the influence of the rotation rate on the averaged flow properties is depicted in figure 4. The temporal, azimuthal and axial averaged angular velocity profiles are given

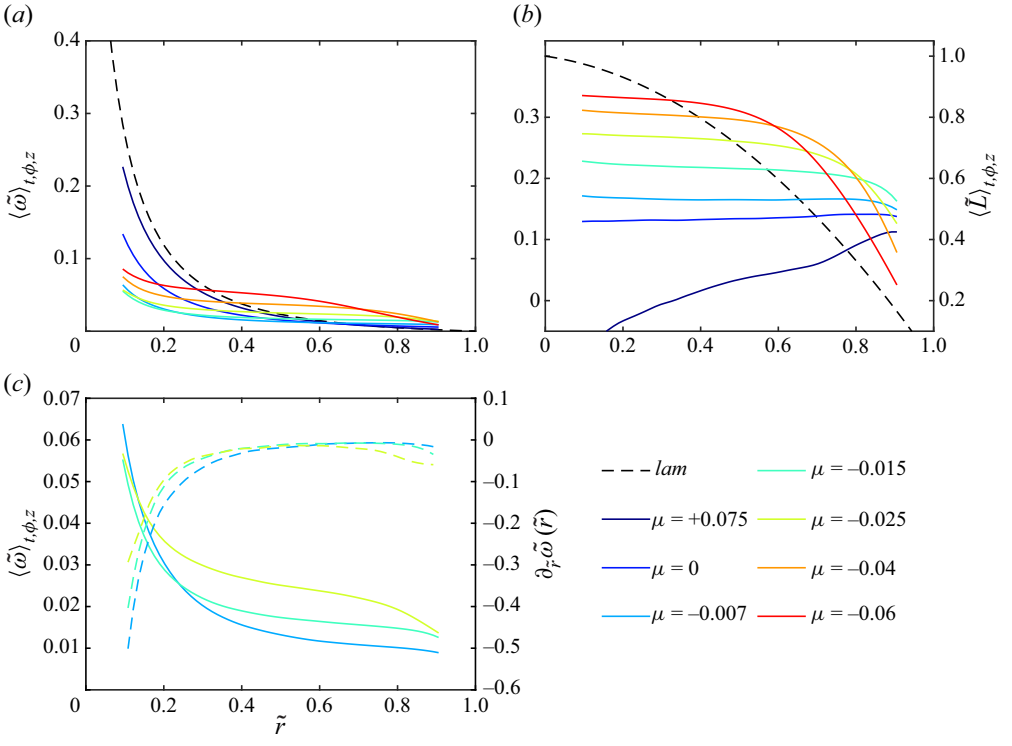


Figure 4. Radial Profiles of spatially and temporally averaged $(t, \phi, z)$ normalized angular velocity $\tilde{\omega}$ $(a)$ and normalized angular momentum $\tilde{L}$ $(b)$ for $Re_s = 6.1 \times 10^4$ and different rotation ratios $\mu$. The dashed line in $(a,b)$ denotes the corresponding laminar profile (cf. (3.4), (3.5)). $(c)$ Magnification for $\tilde{\omega}$ profiles, and the radial gradient of $\tilde{\omega}(\tilde{r})$, for $\mu = -0.007, -0.015, -0.025$.

in figure 4$(a)$ for $Re_s = 6.1 \times 10^4$ and for the rotation ratio $-0.06 \leq \mu \leq +0.008$, where the laminar profile is also plotted for comparison. The profile related to the co-rotating regime approximately follows the laminar profile quite well, but the profiles deviate from the laminar profile for pure inner rotation and counter-rotation. The profiles tend to become flatter in the bulk flow until the gradient is lowest around $-0.015 \leq \mu \leq -0.007$. For higher counter-rotation, the profiles are shifted to higher $\tilde{\omega}$ near the inner boundaries.

Figure 4$(b)$ shows the corresponding profiles of the normalized angular momentum $(\tilde{L})$ for the same driving parameters. In the presentation of $\tilde{L}$ one has to consider that $(L_1 - L_2)$ differs a lot with $\mu$, especially close to the Rayleigh stable area, where it tends to be zero, resulting in $\tilde{L}$ being large. The behaviour of the angular momentum across the gap for the co-rotation case shows a unique behaviour compared with the other studied cases, where $\langle\tilde{L}\rangle_{t,\phi,z}$ has a positive slope varying through $\tilde{r}$. For weak counter-rotating cases, the profiles are flat in the bulk with different values, but as the counter-rotation increases, the flat radial profiles of $\langle\tilde{L}\rangle_{t,\phi,z}$ exhibit a strong negative slope starting from a specific radial position, and the position of this inflection point moves toward the inner part of the gap as the counter-rotation increases. The position of this inflection point can be related to the position of the neutral line, which will be discussed in detail in § 3.3.

Figure 5 shows the radial profile of the fluctuation intensity, measured by the root mean square (r.m.s.), of the radial velocity multiplied by $2\pi r$ and the angular momentum (L)

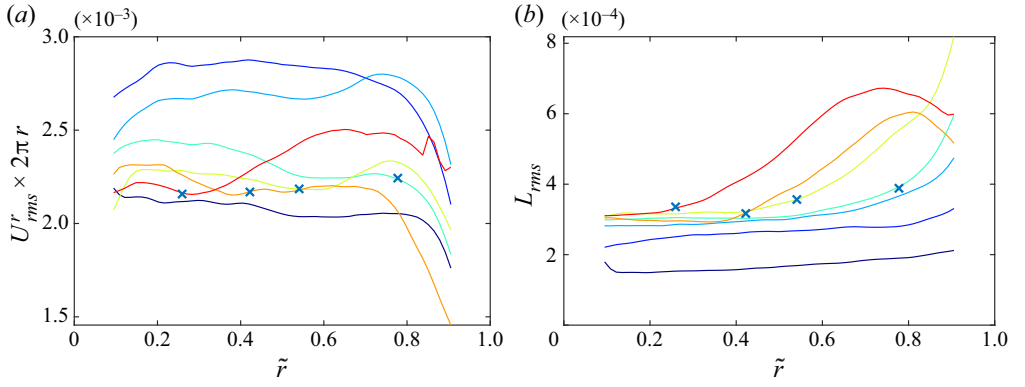


Figure 5. Radial profiles of spatially and temporally averaged $(t, \phi, z)$ root mean square (r.m.s.) of $(a)$ the radial velocity fluctuation multiplied by $2\pi r$, and $(b)$ angular momentum fluctuation, for different rotation ratios and $Re_s = 6.1 \times 10^4$. The crosses indicate the radial position of the neutral surface presented in figure 7. The legends used in this figure are the same as in figure 4.

r.m.s. for different rotation ratios. The r.m.s. is calculated for the value $U = u - \langle u \rangle_t$. According to the incompressibility condition, a radial inflow or outflow decreases in magnitude with the circumference. We compensate for this for better readability of the graph by multiplying $U^r_{rms}$ by $2\pi r$. Thus, in the case of a radially confined inflow and outflow region, where the mass flux in the radial direction is constant (like a large-scale circulation or time-dependent oscillations), the profile experiences a flat behaviour and $2\pi r U^r_{rms}$ quantifies the strength of the radial fluctuations. Figure 5$(a)$ shows these radial profiles of $U^r_{rms}$ by $2\pi r$ for different rotation ratios. For $\mu = +0.007$, 0 and $-0.007$, the profile is almost flat in the bulk, whereas $\mu = 0$ and $-0.007$ experience higher values across the gap. For the stronger counter-rotating cases, the profiles show a different behaviour, where the fluctuation profile experiences two different plateaus and a transition region in between. Inside the bulk flow close to the inner cylinder, the strength of the radial fluctuations quantified by $2\pi r U^r_{rms}$ is observed to be less compared with the strength of the radial fluctuations of the flow close to the outer cylinder. The radial position where the behaviour changes from the inner region to the transient region coincides approximately with the neutral surface, as determined in figure 7 (the radial position where the azimuthal velocity vanishes). The same can be said about the angular momentum fluctuation ($L_{rms}$) shown in figure 5$(b)$, where the profiles for $\mu = +0.007$, 0 and $-0.007$ are mostly flat in the bulk, while for higher counter-rotation ratios, they are flat until they reach the radial position of the neutral velocity (no mean angular momentum). Furthermore, in the outer part of the gap the angular momentum fluctuation increases toward a strong maximum. At the cylinder walls, the fluctuation has to be zero due to the no-slip boundary condition.

To focus more on the counter-rotating regimes with low rotation ratio, where the angular momentum transport is expected to increase and achieve a maximum, and which will be proven and discussed in detail in § 4.1, figure 4$(c)$ shows the radial profile of $\langle \tilde{\omega} \rangle_{t,\phi,z}$ and $\partial_{\tilde{r}} \tilde{\omega}(\tilde{r})$ for $\mu = -0.007$, $-0.015$ and $-0.025$ to have a close look at the angular velocity gradient. All three cases show the lowest gradient in the centre of the bulk compared with the other cases, but for the $\mu = -0.025$ case, a more negative slope is observed compared with both $\mu = -0.007$ and $\mu = -0.015$ cases, also, $\mu = -0.007$ has a clear increase in gradient in the inner region. Inspecting the radial profile of the radial gradient of $\tilde{\omega}(\tilde{r})$ one can clearly observe this low gradient in the bulk, where at $0.6 \leq \tilde{r} \leq 0.8$ the value of

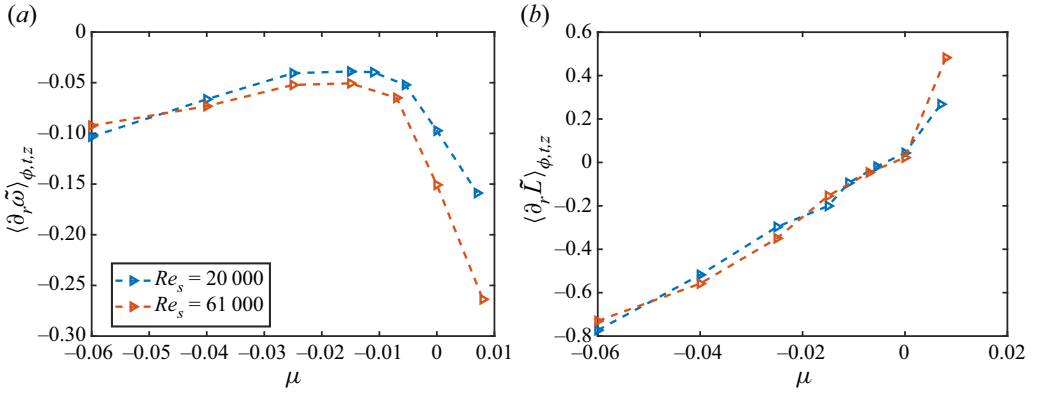


Figure 6. (*a*) Normalized radial gradient of angular velocity profiles as a function of $\mu$, (*b*) normalized radial gradient of angular momentum profiles as a function of $\mu$. Blue and orange triangles represent the results of $Re_s = 20\,000$ and $Re_s = 6.1 \times 10^4$ for different rotation ratios, respectively.

$\partial_{\tilde{r}} \tilde{\omega}(\tilde{r})$ for $\mu = -0.007$ and $\mu = -0.015$ is mostly zero, which means that at these radial positions $\langle \tilde{\omega} \rangle_{t,\phi,z}$ is constant.

To further quantify the smallest gradient of the $\langle \tilde{\omega} \rangle_{t,\phi,z}$ in the bulk, the gradient is calculated along $0.1 < \tilde{r} < 0.9$. The gradient is directly evaluated from the velocity profiles. The normalized radial gradient of angular velocity shown in figure 6(*a*) is negative for all rotation ratios and for both $Re_s$. Both curves in the figure show the smallest value of gradient for $-0.02 \leq \mu \leq -0.007$, and the increase in gradient magnitude depends on the $Re_s$. Figure 6(*b*) shows the radial gradient of the $\langle \tilde{L} \rangle_{t,\phi,z}$ in the bulk, where also the $\langle \tilde{L} \rangle_{t,\phi,z}$ exhibits the smallest radial gradient for low counter-rotating cases. The two curves shown in both figures are related to two different experiments with different shear Reynolds numbers; however, both curves show the same behaviour but with slightly different values. Thus, it is shown that the gradient values are more dependent on the rotation ratio than on the shear Reynolds number.

### 3.3. *Neutral surface*

The neutral surface is defined as the radial location in the gap where the azimuthal velocity component $u_\phi$ vanishes. The velocity profile and particularly the azimuthal velocity ($u_\phi$) profile give access to finding the radial position of the neutral surface by detecting the position where the mean azimuthal velocity changes its direction (sign).

The neutral surface exists just for counter-rotating cases, and it coincides with the outer cylinder for pure inner cylinder rotation, while for the co-rotating cases, the neutral surface is not defined as both cylinders are rotating in the same direction. This surface indicates the division between the stable and unstable regions and implies a detachment of the unstable flow for any $\mu < 0$. In the stable region any perturbation to the azimuthal flow decay is directly damped by the mean azimuthal flow, where the radial position of the neutral surface ($r_n$) is defined according to Chandrasekhar (1961) as

$$r_{n,inv}(\mu) = r_1 \sqrt{\frac{1-\mu}{\eta^2 - \mu}}. \tag{3.6}$$

But experiments and viscous calculations show that large-scale circulation (LSC) patterns can extend beyond this neutral surface when counter-rotation sets in. Esser &

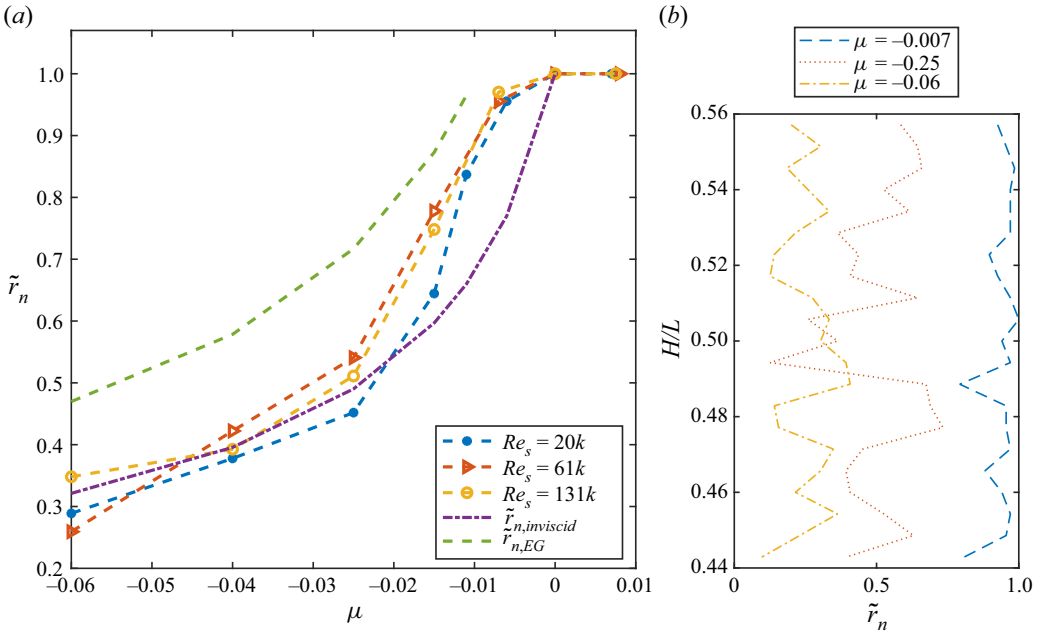


Figure 7. (*a*) Normalized neutral surface $\widetilde{r_n}$ as a function of the rotation ratio $\mu$ for $Re_s = 20\,000$ (black), $Re_s = 6.1 \times 10^4$ (red) and $Re_s = 1.31 \times 10^5$ (yellow). (*b*) The radial position of the neutral surface at different heights for $Re_s = 6.1 \times 10^4$ and $\mu = -0.007, -0.025, -0.06$.

Grossmann (1996) deduced from their stability calculation a prediction for the vortex extension called $r_{n,EG}$, and that flow structures emerge in the neutral surface by a factor of $a(\eta)$,

$$r_{n,EG}(\mu) = r_1 + a(\eta)(r_{n,inv} - r_1); \quad a(\eta) = (1-\eta)\left[\sqrt{\frac{(1+\eta)^3}{2(1+3\eta)}} - \eta\right]^{-1}. \quad (3.7a,b)$$

Due to the extension of the secondary flow to the outer cylinder wall, intermittency evolves, causing radial inhomogeneity inside the gap. The onset of the intermittency was used by Brauckmann & Eckhardt (2013) to predict the parameter of the torque maximum and was experimentally validated by Merbold *et al.* (2013) and Froitzheim *et al.* (2017) for $\eta = 0.5$, and Froitzheim *et al.* (2019*b*) for $\eta = 0.357$. Figure 7(*a*) shows the position of the normalized neutral line for the three different shear Reynolds numbers, and for the different rotation ratios studied in the current study. The curves are depicted together with the two predictions introduced above. For the three curves shown in figure 7, it is clear that the neutral line does not exist for all experiments with $(0 \leq \mu)$ as mentioned above. The detachment of the neutral line from the outer cylinder started for the low counter-rotation cases. The position of the detachment point for the different $Re_s$ did not converge with either of the two predictions, and this can be explained by the patterns, which do not fill the entire gap as they do in the observations by Froitzheim *et al.* (2017), Ostilla-Monico *et al.* (2014), Huisman *et al.* (2014). These results differ in the flow in the very wide gap ($\eta = 0.1$) in contrast to TC flow in narrower geometries. As an example, Froitzheim *et al.* (2017) and Brauckmann & Eckhardt (2013) showed that the detachment of the neutral line from the outer wall was well predicted by the prediction of Esser &

Grossmann (1996) for $\eta = 0.5$ and $\eta = 0.71$, respectively. It is clear in the very wide gap geometry studied here that the detachment of the neutral line starts once the outer cylinder is set in counter-rotation. The outer cylinder radius is 10 times larger than the inner one in the TC geometry used in the current study; this can explain the ability of the outer cylinder rotation to stabilize the unstable fluid next to it once it is set to rotation, although at very low rates, as shown in 7(*a*) for $\mu = -0.0077$. For higher counter-rotating cases, the observed neutral position coincides with the prediction of the inviscid fluids.

Figure 7(*b*) shows how the position of the neutral surface depends on the height. Here the deviation of the neutral position with height is observed, which is caused by the difference in the secondary flow ($u_r$, $u_z$ where only $u_r$ is measured) between the different heights. Figure 3 shows the alternating strong inflow and outflow for the measured heights. Also from figure 7(*b*) it can be observed that the $\tilde{r}_n$ profile has a certain kind of periodicity over the different heights for the presented rotation ratios. The variation of $\tilde{r}_n$ along the different heights is the highest for $\mu = -0.025$. The low value of the variation of $\tilde{r}_n$ for $\mu = -0.007$ can be returned to the fact that the neutral line is just beginning to detach, where in some heights it is shown that the position of the neutral line is still attached to the outer cylinder. For $\mu = -0.06$, small axial variation is also observed due to the stabilization effect of the rotation of the outer cylinder, so the unstable region is confined near the inner cylinder.

## 4. Angular momentum transport

### 4.1. *The Nusselt number*

Beforehand, the flow field dependence on the different parameters, like the shear Reynolds number $Re_s$ and the rotation ratio $\mu$, is shown. In this section the angular momentum current $J^\omega$ is analysed in terms of the Nusselt number. The angular momentum transport is the conserved transport quantity in TC flow, and is defined according to the Eckhardt–Grossmann–Lohse (EGL) theory (Eckardt *et al.* 2007) by $J_\omega$ presented in (1.2). At the cylinder walls, $\langle u_r\omega\rangle_{A(r),t}$ vanishes, and $J^\omega$ results from the friction exhibited to the walls and can be directly measured by the torque acting on the cylinders. In previous studies on various radius ratios, this has been determined by measuring the torque at the cylinders, while in this study the torque is too small for an accurate measurement system. In this study, $J^\omega$ is calculated using the velocity field measured by PIV. The measure of the angular momentum transport is then defined by the quasi-Nusselt number,

$$Nu_\omega = \frac{J^\omega}{J^\omega_{lam}}, \tag{4.1}$$

where $J^\omega_{lam} = 2\nu r_1^2 r_2^2(\omega_1 - \omega_2)/(r_2^2 - r_1^2)$ results from the laminar Couette solution (3.4).

According to the theory derived by EGL the transverse current of azimuthal motion $J_\omega$ is constant over all radii. Figure 8(*a*) shows the measured Nusselt number radial profiles $Nu_\omega(\tilde{r})$ for different rotation rates and $Re_s = 1.31 \times 10^5$ normalized by its radial average. It can be observed that the radial profiles in the radial range $\tilde{r} \in [0.2, 0.7]$ scatter around 1, in the limits between [0.85, 1.15], which is considered to be in good agreement with the definition of the independence of the angular momentum flux on the radial position. Although the profiles are not exactly flat, it should be taken into consideration that these results are calculated from PIV measurements, where spatial resolution limitations always exist. It remains part of the uncertainty when studying the angular transport in this study that not all small scales are resolved. Another uncertainty is the instantaneous LSC, which is not covered by the current measurements and may also influence the results.

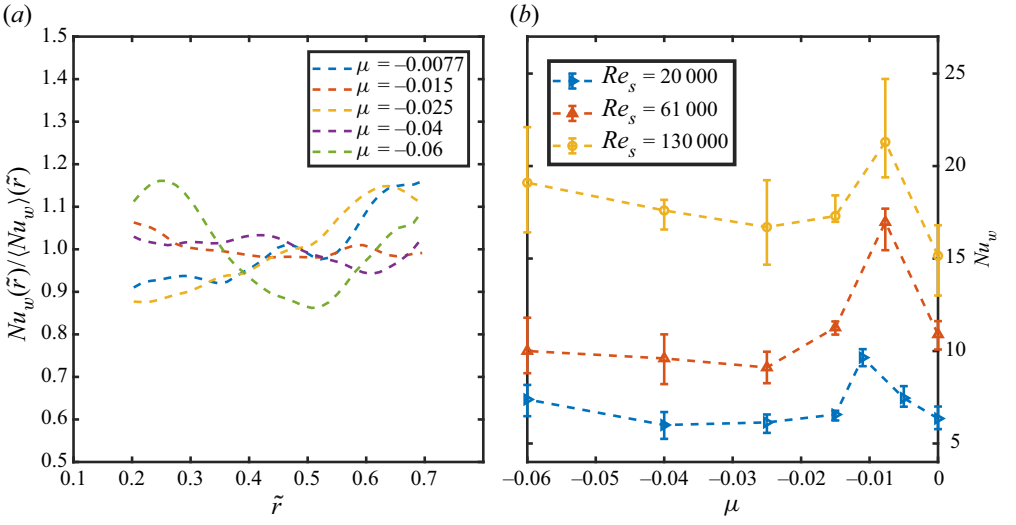


Figure 8. (*a*) The quotient of the Nusselt number radial profiles over its average in the radial range for different rotation rates $\mu$, at a fixed shear Reynolds number $Re_S = 1.31 \times 10^5$. (*b*) The variation of the radial averaged Nusselt number $Nu_\omega^{Total}$ as a function of $\mu$ for different shear Reynolds numbers.

However, an axial domain up to 2d is covered by our measurements, and figure 3 shows the existence of an LSC of size $\approx 0.43d$, which indicates that the axial dependence of the flow is mostly covered by our measurements, and it can be concluded that the influence of not covering the instantaneous LSC is small. To further improve the certainty of LSC, a 3-D measurement would be a solution. But besides the difficulty of collecting the necessary equipment for such measurement methods (several high-speed and highly resolved cameras and optical equipment plus a new high-power light source), the 3-D measurements reduce the resolution of small-scale fluctuations significantly and, as a result, reduce spatial resolution drastically (Tokgöz *et al.* 2012). On the other hand, if a method is used to resolve small scales by the use of magnification, the LSC will not be covered. Taking all these factors into consideration and having a measurement method that covers the largest possible variety of flow scales, the angular momentum transport in this study is measured using a method already validated by Froitzheim *et al.* (2017) using the same TC facility but with a different radius ratio $\eta = 0.5$, where it shows very high accuracy. The $Nu_\omega$ is calculated at all gap radial positions, although the angular momentum transport can be calculated by measuring the azimuthal and radial velocities at a singular point, as done by Ji *et al.* (2006) and Burin, Schartman & Ji (2010) when studying the wide gap TC geometry $\eta = 0.35$, using the 2-D laser Doppler velocimetry method. But in order to enhance the certainty through statistics, the transport was calculated at the different gap radial positions and averaged across the bulk area. As close to the cylinder walls, the boundary layer will increase small-scale fluctuations induced in the shear, which are not resolved by the used method. Thus, an averaging interval of $Nu_\omega$ in the radial range $\tilde{r} \in [0.2, 0.7]$ is used to ensure higher accuracy.

The dependence of the Nusselt number $Nu_\omega$ on both the rotation ratio and the shear Reynolds number is studied in figure 8(*b*), where the variation of the radial averaged Nusselt number is plotted for three different $Re_s$ values ($Re_s = 20\,000$, $6.1 \times 10^4$ and $1.31 \times 10^5$) with respect to different rotation rates in the counter-rotating regime.

The uncertainty bars in the figure show the maximum and minimum values of $Nu_\omega$ in the radial domain $0.2 < \tilde{r} < 0.7$, where $Nu_\omega(\tilde{r})$ is radially averaged. Using the measured $Nu_\omega$ a separation is defined, so the counter-rotating rates with $-0.012 \leq \mu \leq 0$ are named low counter-rotating regimes, $-0.025 \leq \mu \leq -0.015$ are named moderate counter-rotating regimes and, for $\mu \leq -0.04$, high counter-rotating regimes. However, when the low counter-rotating cases in the current study are compared with other studies with different radius ratios, we are not comparing the exact values of $\mu$ between both studies but we are comparing the different regimes according to the Nusselt behaviour.

From the presented $Nu_\omega$ in figure 8(*b*), first a common behaviour between the different studied cases with different $Re_s$ is observed, where it is obvious that $Nu_\omega$ achieves its maximum value in the area of low counter-rotation. So for $Re_s = 20\,000$, the rotation ratio where the $Nu_\omega$ achieved its maximum value is determined at $\mu_{max} = -0.011$. While for $Re_s = 6.1 \times 10^4$ and $Re_S = 1.31 \times 10^5$, the maximum value of $Nu_\omega$ is determined at $\mu_{max} = -0.0075$. In this study, as the PIV measurements are used to calculate the Nusselt number, we are not able to calculate $Nu_\omega$ at a very large range of $\mu$ so we can determine an exact value for $\mu_{max}$. As an example, for $Re_s = 1.31 \times 10^5$, $6.1 \times 10^4$, the flow in the low counter-rotating regime for rotation ratios $\mu = -0.0075, -0.015$ is measured, where it shows $\mu_{max} = -0.0075$. For $Re_s = 20\,000$, and for the same regime, the rotation ratios $\mu = -0.006, -0.011, -0.015$ are measured, and it shows $\mu_{max} = -0.011$. So a general conclusion can be drawn from the studied cases, that $\mu_{max}$ is determined for rotation ratios between $-0.012 \leq \mu_{max} \leq -0.007$.

From previous works like those done by Merbold *et al.* (2013) and Froitzheim *et al.* (2017) and then by Froitzheim *et al.* (2019*b*), the maximum $\mu_{max}$ was found to be $\mu_{max} = -0.2 \pm 0.02$ for $\eta = 0.5$ and $\mu_{max} = -0.123 \pm 0.03$ for $\eta = 0.357$, respectively, which showed that $\mu_{max}$ is shifted toward less counter-rotating values for wider gaps. The results of the current study support this idea too. Another observation is investigated here, which agrees with the results for $\eta = 0.5$ and $\eta = 0.357$, that at $\mu_{max}$ the normalized radial gradient angular velocity profiles achieve minimum through the bulk, as shown in figure 6(*a*), where it is clear for both curves related to $Re_s = 20\,000$ and $Re_s = 6.1 \times 10^4$ that the minimum gradient is in the area of $-0.0077 \leq \mu \leq -0.015$, where $\mu_{max}$ lies in this domain. The results show a common behaviour with the previous studies done for narrower gaps, where they showed that as the counter-rotation is increased beyond the maximum $\mu < \mu_{max}$, the value of the Nusselt number decreases. This is explained by the fact that the rotation of the outer cylinder stabilizes the flow in the outer region, and the enhanced LSC cannot fill the entire gap width, so the transport is suppressed. But in huge contrast to the results achieved for $\eta \geq 0.357$, in the current study we observe from figure 8(*b*) that $Nu_\omega$ first decreases for $\mu < \mu_{max}$, but then it achieves a minimum $\mu_{min}$, and by increasing the counter-rotation further $\mu < \mu_{min}$ the $Nu_\omega$ tends to increase again.

The results show a dependence between the position of $\mu_{min}$ and the shear Reynolds number. As $Re_s$ increases, the position of $\mu_{min}$ shifts toward the low counter-rotating regime. So for $Re_s = 20\,000$, $\mu_{min} = -0.04$ is found, and for $Re_s = 6.1 \times 10^4$, $\mu_{min} = -0.025$, while for $Re_s = 1.31 \times 10^5$, $\mu_{min}$ can not be exactly determined. However, it is clear that it exists for $-0.025 < \mu < -0.015$. While $\mu_{max}$ is independent of $Re_s$, the minimum $\mu_{min}$ shows a clear dependence on the shear Reynolds number. As a conclusion, the angular momentum transport shows a maximum at low counter-rotating regimes, and a second maximum is expected for higher counter-rotating regimes, as at infinite counter-rotation one can assume a pure outer cylinder rotation with a low $Nu_\omega$. This behaviour is in contrast to what is reported for TC flows with $\eta \leq 0.9$ where the maximum of angular momentum transport is found at one defined rotation ratio, where it

is accompanied by the strengthening of the large-scale structures, which is also the case here for the first maximum.

A similar double maxima behaviour of the angular momentum transport observed for the currently studied TC geometry is observed on the extreme opposite side of the TC geometry, the very narrow gaps ($\eta > 0.91$) (Brauckmann *et al.* 2016; Ezeta *et al.* 2020) and the RPC flow (Salewski & Eckhardt 2015; Kawata & Alfredsson 2016), where for such geometries, they reported the existence of two $Nu_\omega$ maxima at different rotation rates. The first maximum, or what they called 'the broad peak', was accompanied by the strengthening of the large-scale structures and a second maximum, 'the narrow peak', which is a consequence of shear instabilities. The first maximum observed in all TC geometries ($0.1 \leq \eta \leq 0.98$) and RPC flows can be attributed to the same reason, the strengthening of the large-scale structures. But, concerning the second expected maximum observed in the current study for $\eta = 0.1$ and the 'narrow peak', it is hard to assume that both these peaks are a consequence of the same instability. In addition, Ezeta *et al.* (2020) shows that as the driving of the system varies, the broad peak remains roughly at the same rotation ratio, which is in agreement with what is observed in the current study for the first $Nu_\omega$ maximum. Furthermore, they show that the narrow peak position is dependent on the driving rate, which can also be the case for the second expected maximum in this study, as it is observed here that $\mu_{min}$ is $Re_s$ dependent, which can lead the position of the second maximum to be $Re_s$ dependent too.

In order to further understand the behaviour of the Nusselt number with the different parameters ($Re_S$ and $\mu$), the flow velocity field is decomposed according to Brauckmann & Eckhardt (2013),

$$\boldsymbol{u} = \langle \boldsymbol{u} \rangle_t + \boldsymbol{u}' = \bar{\boldsymbol{u}} + \boldsymbol{u}', \tag{4.2}$$

where $u'$ denotes the turbulent fluctuations and $\bar{u}$ is the temporal-averaged velocity. The decomposition of the flow field shown in (4.2) is used in order to decompose the Nusselt number into two values, one related to the mean large-scale contribution $Nu_\omega^{LSC}$ and the second related to the turbulent contribution $Nu_\omega^{Turb}$. So that the Nusselt number reads

$$Nu_w = Nu_w^{LSC} + Nu_w^{Turb}, \tag{4.3}$$

with

$$Nu_w^{Turb} = J_{lam}^{-1} \langle r^3 \langle u_r' \omega' \rangle_{A(r),t} \rangle_r, \tag{4.4}$$

$$Nu_\omega^{LSC} = J_{lam}^{-1} \langle r^3 (\langle \bar{u}_r \bar{\omega} \rangle_{A(r),t} - \nu \partial_r \langle \bar{\omega} \rangle_{A(r),t}) \rangle_r, \tag{4.5}$$

where the mixed terms $\langle \bar{u}_r \omega' \rangle_{A(r),t}$ and $\langle \bar{\omega}_r u_r' \rangle_{A(r),t}$ vanish (cf. Froitzheim *et al.* 2017). Also the term $\partial_r \langle \omega' \rangle_{A(r),t}$ vanishes as they are all linear in the deviation quantities (Brauckmann & Eckhardt 2013).

In figure 9 the variation of both contributions of Nusselt number as a function of $Re_s$ and $\mu$ is studied. Figure 9($a$) shows the radial averaged Nusselt number large-scale contribution $Nu_\omega^{LSC}$ as a function of $\mu$ and $Re_s$. For $Re_s = 20\,000$, $6.1 \times 10^4$ and $1.31 \times 10^5$, the $Nu_\omega^{LSC}$ shows the highest value at $\mu_{max}$ (which is in agreement with the previous investigation, Froitzheim *et al.* 2017), where the large-scale circulation enhances the angular momentum transport. Then $Nu_\omega^{LSC}$ decreases for stronger counter-rotation as the detachment of the neutral line from the outer wall starts, so the circular patterns are more pushed toward the inner region of the gap, which leads to a decrease in the Nusselt number. Figure 9($a$) shows that $Nu_\omega^{LSC}$ decreases for $\mu < \mu_{max}$ until it reaches a level where the contribution of $Nu_\omega^{LSC}$ varies weakly with the rotation rate, and tends to be independent of the rotation rates.

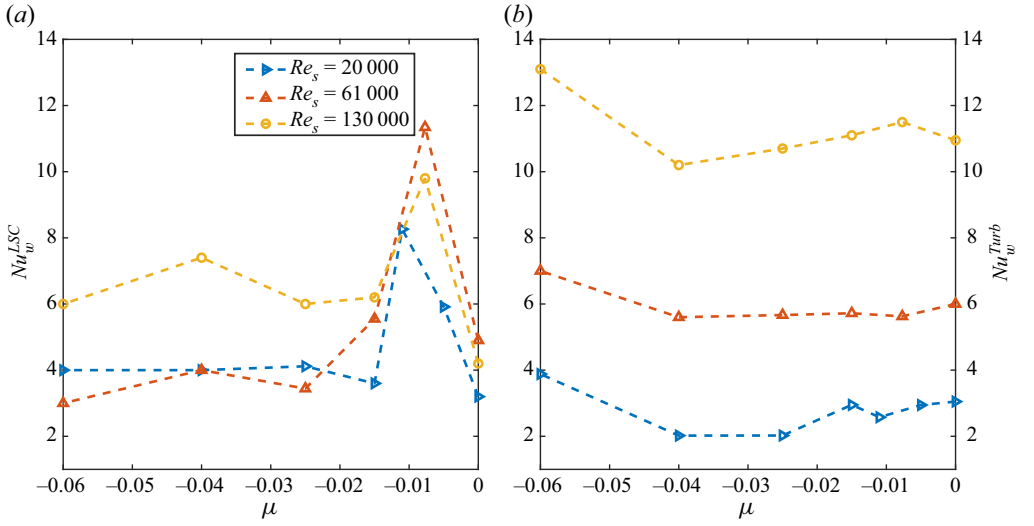


Figure 9. The Nusselt number $Nu_\omega$ is decomposed into its large-scale contribution ($Nu_\omega^{LSC}$) and turbulent contribution ($Nu_\omega^{Turb}$). (*a*) Radial averaged Nusselt number large-scale contribution ($Nu_\omega^{LSC}$), (*b*) radial averaged Nusselt number turbulent contribution ($Nu_\omega^{Turb}$) as a function of $\mu$, for different shear Reynolds numbers.

Figure 7(*a*) shows how the position of the neutral line changes for higher counter-rotating flows. These findings are in strong contrast to what was investigated for $\eta = 0.5$ and $\eta = 0.357$, where it was shown that $Nu_\omega^{LSC}$ decreases for higher counter-rotating cases.

It is important to also understand the contribution of turbulence to global transport, quantified by the value $Nu_\omega^{Turb}$. Figure 9(*b*) shows the radial averaged turbulent contribution to the Nusselt number $Nu_\omega^{Turb}$ as a function of $\mu$ and $Re_s$. The $Nu_\omega^{Turb}$ shows a small variation in the values along the different low counter-rotating cases for constant $Re_s$, but a clear increase for the high counter-rotation case. As a comparison between figures 9(*a*) and 9(*b*), for $Re_s = 20\,000$, it is shown that the contribution of $Nu_\omega^{LSC}$ in the $Nu_\omega^{Total}$ is dominant in contrast to $Nu_\omega^{Turb}$ , while for $Re_s = 6.1 \times 10^4$, the contributions are mostly equal and, finally, for $Re_S = 1.31 \times 10^5$, the contribution of $Nu_\omega^{Turb}$ has increased much more than that of $Nu_\omega^{LSC}$. So it can be stated that as the shear Reynolds number increases, the intensity of the turbulent contribution in the flow increases strongly, while the $Nu_\omega^{LSC}$ is increasing only slightly with $Re_s$.

### 4.2. *Spatial and temporal behaviour of the shear stress*

Figures 10–12 show the space–time diagram of the shear stress component $\omega u_r$ multiplied by $r^3$ and divided by $J_{lam}$ for different rotation ratios in the $\phi - t$ plane for $Re_s = 6.1 \times 10^4$. For each rotation ratio, the space–time diagram is considered for the different measured axial positions, but as they show mostly the same behaviour and for simplicity, one axial height is selected for representation, where the selected height $r^3(u_r\omega)$ has the highest intensity compared with other heights. Understanding the spatial–temporal behaviour will also give us the opportunity to compare and reveal the influence of the rotation ratio on the shear stress and angular momentum transport. The figures depict the contour plot of the space–time diagram at five radial positions distributed along the gap. The top subfigures belong to radial positions close to the inner cylinder, and the

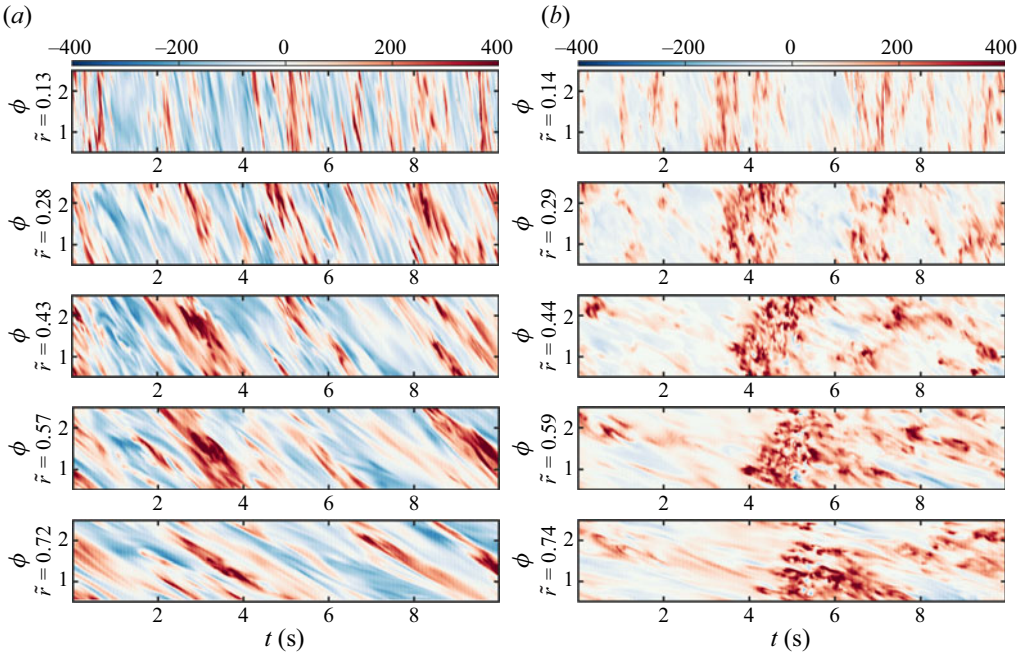


Figure 10. Contour plot showing the space–time diagram of $r^3(\omega u_r)/J_{lam}$ in the azimuthal-time plane for five different radial positions, at (*a*) $\Delta z = +12$ mm, (*b*) $\Delta z = +4$ mm from apparatus mid-height, for $Re_s = 6.1 \times 10^4$ for the pure inner cylinder and low counter-rotating cases. The top figure is a radial position close to the inner cylinder, and the bottom figure is close to the outer cylinder. Results are shown for (*a*) $\mu = 0$ and (*b*) $\mu = -0.0077$.

bottom subfigures belong to radial positions close to the outer cylinder. It is noteworthy that the range of $\phi$ is kept constant for this representation, which has a strongly increasing circumferential length $r\phi$ as the radius increases.

Equation (1.2) can be separated into two terms: the first term represents the convective term $r^3 < u_r\omega >_{A(r),t}$ and the second represents the viscous term $r^3\nu\partial_r\langle\omega\rangle_{A(r),t}$. In the bulk flow where our analysis takes place, the convective term is the dominant term, as the contribution of the viscous term does not exceed 5 % of the total $J_\omega$ in the bulk. For the stated reason, $r^3(u_r\omega)$ is chosen for the comparison between the different experiments with different rotation ratios. Furthermore, $r^3(u_r\omega)$ is divided by $J_{lam}$ so the values can then be compared with the values in figure 8. The space–time evolution of $r^3(u_r\omega)/J_{lam}$ is analysed in detail in figures 10–12 as it is the main contributor to the $Nu_\omega$ when averaged over $\langle\rangle_{A(r),t}$, which is represented by the depiction in the $\phi - t$ plane.

From the underlying data, the effort is to study the existence of travelling patterns through the gap, and in the case of their existence, to see their intensity and the direction of propagation. Inspecting the space–time behaviour leads to an understanding of how turbulent structures behave throughout the gap and quantifies the transported angular momentum. So for the shown figures, the red and blue spots are considered to be related to a propagating pattern, which can be a LSC down to a small-scale turbulent pattern that travels through the gap. Red patterns represent shear stresses that transport angular momentum outwards (positive), while blue patterns transport momentum in the opposite direction.

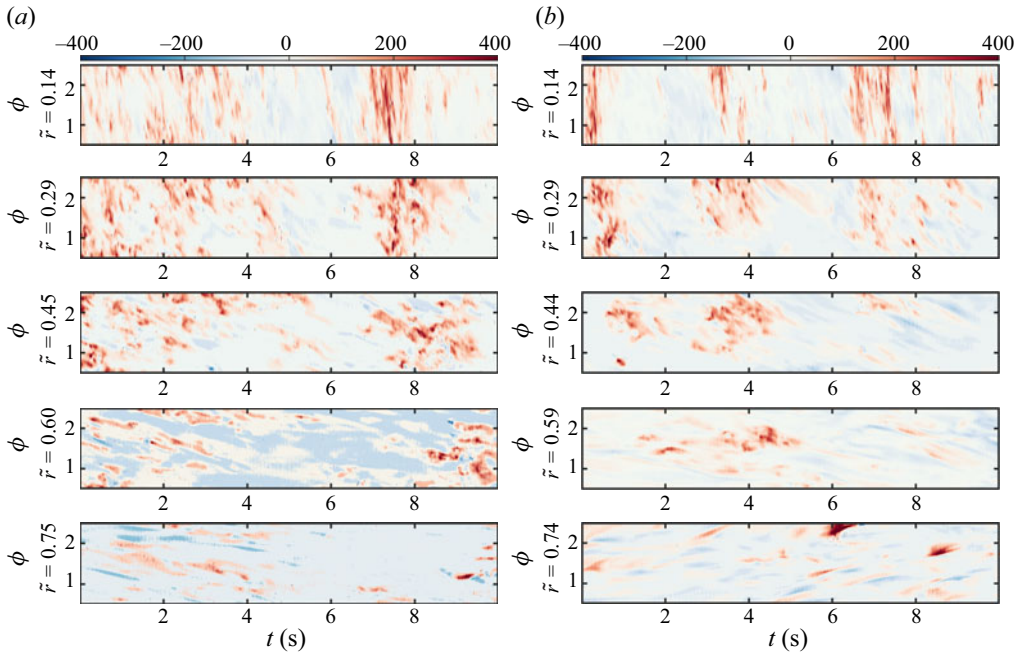


Figure 11. Contour plot showing the space–time diagram of $r^3(\omega u_r)/J_{lam}$ in the azimuthal-time plane for five different radial positions, at (*a*) $\Delta z = 0$ mm, (*b*) $\Delta z = +8$ mm from apparatus mid-height, for $Re_s = 6.1 \times 10^4$ for counter-rotating cases. The top figure is a radial position close to the inner cylinder, and the bottom figure is close to the outer cylinder. Results are shown for (*a*) $\mu = -0.015$ and (*b*) $\mu = -0.025$.

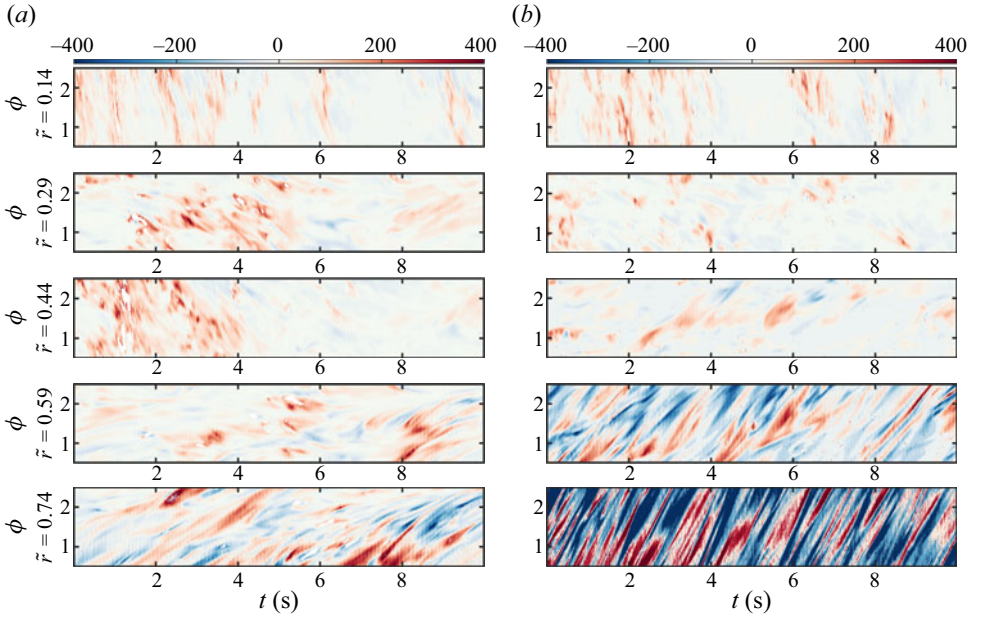


Figure 12. Contour plot showing the space–time diagram of $r^3(\omega u_r)/J_{lam}$ in the azimuthal-time plane for five different radial positions, at (*a*) $\Delta z = +4$ mm, (*b*) $\Delta z = +4$ mm from apparatus mid-height, for $Re_s = 6.1 \times 10^4$ for high counter-rotating cases. The top figure is a radial position close to the inner cylinder, and the bottom figure is close to the outer cylinder. Results are shown for (*a*) $\mu = -0.04$ and (*b*) $\mu = -0.06$.

Starting with the pure inner cylinder rotating case, figure 10(*a*) shows the existence of propagating patterns with a short time scale. The last is deduced from the thickness of the red positive transporting patterns in the time axis, which is relatively small. The existence of these patterns with short lifetimes can explain the moderate contribution of $Nu_\omega^{LSC}$ in $Nu_\omega^{Total}$ shown in figure 9(*a*). When the outer cylinder is set to rotate slightly in the opposite direction of the inner cylinder rotation, different behaviour is observed. The positive spots, which are related to the travelling patterns, appear in the flow, but with a longer lifetime than the one we detected for $\mu = 0$. Figure 10(*b*) shows the space–time diagram of $r^3(u_r\omega)$ for $\mu = -0.0077$, where the maximum Nusselt number is found (see § 4). The patterns here can explain this maximum value of the Nusselt number. The existence of patterns with high intensity and long lifetime enhance the transport procedure of angular momentum, so that the $Nu_\omega^{LSC}$ contribution to $Nu_\omega^{Total}$ is the maximum at this rotation ratio compared with other rotation ratios. In contrast to $\mu = 0$, here the huge and long-lasting positive patterns increase the angular momentum transport, and fewer structures of negative transport can be identified.

By increasing the rotation rate of the outer cylinder in the counter direction, the patterns exist with a long lifetime, but in contrast to the $\mu = -0.0077$ case, the intensity of these patterns decreases. Figure 11(*a*,*b*), shows the space–time diagram of $r^3(u_r\omega)$ at $\mu = -0.015$ and $\mu = -0.025$, respectively. Here it is observed how the intensity of these patterns decreases from $\mu = -0.0077$ to $\mu = -0.015$ and then decrease more for $\mu = -0.025$, especially in the radius position near the outer region, which is explained by the stabilizing effect of the outer cylinder rotation. The decrease of the pattern's intensity in these cases causes a decrease in the contribution of $Nu_\omega^{LSC}$ to $Nu_\omega^{Total}$, which leads to a decrease in the total value of $Nu_\omega$ as shown in figure 8.

The dependence of the Nusselt number on the rotation ratio is studied in figures 8 and 9, where the results show an increase in the value of the Nusselt number for higher counter-rotating cases. These results are not in agreement with those related to other TC flows with different radius ratios, like $\eta = 0.5$ and $\eta = 0.357$. Another difference between the currently studied geometry $\eta = 0.1$ and the previously studied geometry with higher radius ratios is the contribution of the $Nu_\omega^{LSC}$ to $Nu_\omega^{Total}$, which did not vary with high values between the different high counter-rotating cases, in contrast to what was shown for $\eta = 0.5$ and $\eta = 0.357$ (Froitzheim *et al.* 2017, 2019*b*). The underlying flow phenomena can be inspected in figure 12, where the space–time diagram of $r^3(u_r\omega)/J_{lam}$ for $\mu = -0.04$ and $\mu = -0.06$ is presented. For the radial positions near the inner region, a behaviour similar to $\mu = -0.015$ and $\mu = -0.025$ is observed, where the patterns with long lifetimes exist but with lower intensity. But the main difference appears in the radial positions near the outer cylinder, where small patterns with a short lifetime but high intensity appear. The intensity of these patterns increases as they go for higher counter-rotating cases. For $\mu = -0.04$, shown in figure 12(*a*), the patterns show lower intensity compared with the patterns shown in figure 12(*b*) for $\mu = -0.06$. The existence of these patterns in the outer regions of the gap can explain why the contribution of $Nu_\omega^{LSC}$ did not decrease with increasing counter-rotation rate, while the intensity of the patterns in the inner region decreased.

In order to study the direction of these propagating patterns, figure 13 shows the space–time diagram of $r^3(\omega u_r)/J_{lam}$ for the lowest and highest counter-rotating rates in the $r - t$ plane at a fixed azimuthal position. The figures are plotted for these two cases, as it is clear from figures 10–12 that the patterns observed for $\mu = -0.007$ appear for all rotation ratios but with lower intensity, and the newly observed patterns in $\mu = -0.06$ also appear in $\mu = -0.04$ but with lower intensity. For $\mu = -0.007$, it is clear from

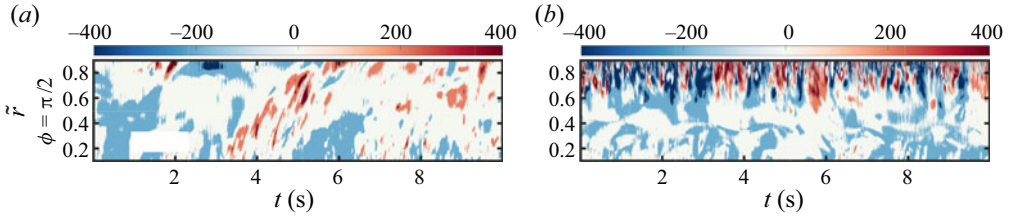


Figure 13. Contour plot showing the space–time diagram of $r^3(\omega u_r)/J_{lam}$ in the radial-time plane at a fixed azimuthal position $\phi = \pi/2$ for $Re_s = 6.1 \times 10^4$, for (*a*) $\mu = -0.007$ and $\Delta z = +4$ mm, and (*b*) $\mu = -0.06$ and $\Delta z = +4$ mm.

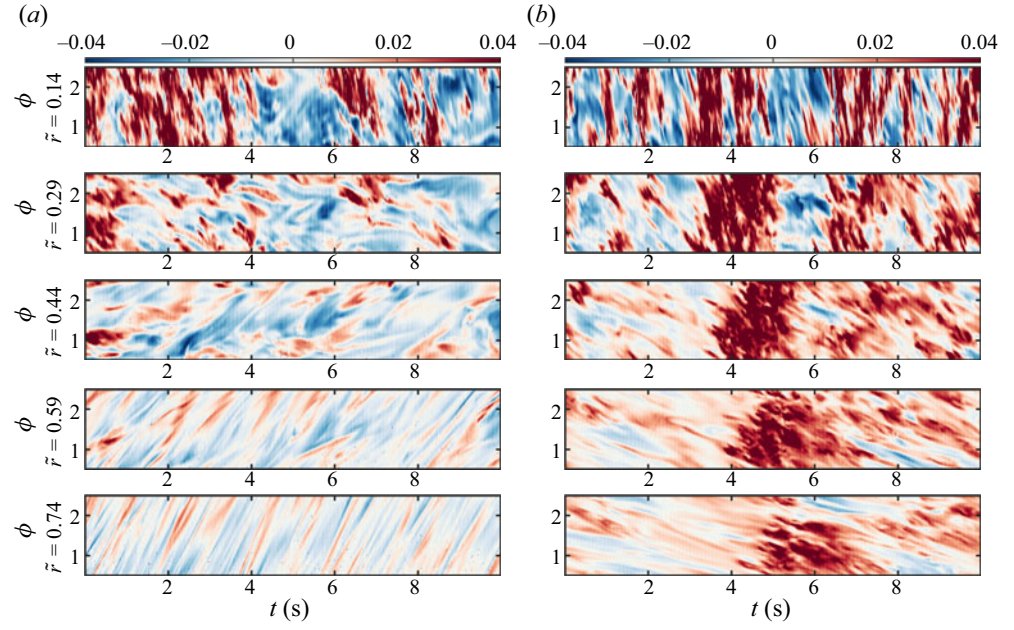


Figure 14. Contour plot showing the space–time diagram of the radial velocity $U_r$ in the azimuthal-time plane for five different radial positions, at (a) $\Delta z = +4$ mm, (*b*) $\Delta z = +4$ mm from apparatus mid-height, for $Re_s = 6.1 \times 10^4$ for (*a*) $\mu = -0.007$ and (*b*) $\mu = -0.06$. The colour map unit is m s$^{-1}$.

figure 13(*a*) that the existing patterns, which are observed in the inner region for all studied rotation rates, are propagating from the inner cylinder toward the outer cylinder. While for $\mu = -0.06$, figure 13(*b*) shows the existence of two sets of patterns, the first set next to the inner cylinder but with low intensity that propagate radially outward, and another set of patterns near the outer cylinder that propagate inward. In addition, figure 14 shows the space–time plots for the radial velocity ($U_r$) at different radial positions and at a fixed height for both $\mu = -0.0077$ and $\mu = -0.06$. For $\mu = -0.077$, the radial velocity decreases in the direction toward the outer cylinder, or in other words, the propagating speed of the patterns decreases as they approach the outer cylinder. The same is observed for $\mu = -0.06$, but here the radial velocity does not vanish in the stable regions near the outer cylinder, although it exists with very low intensity, which means that the newly observed patterns near the outer cylinder travel with lower speed inward in comparison to the patterns propagating outward from the inner regions toward the central area.

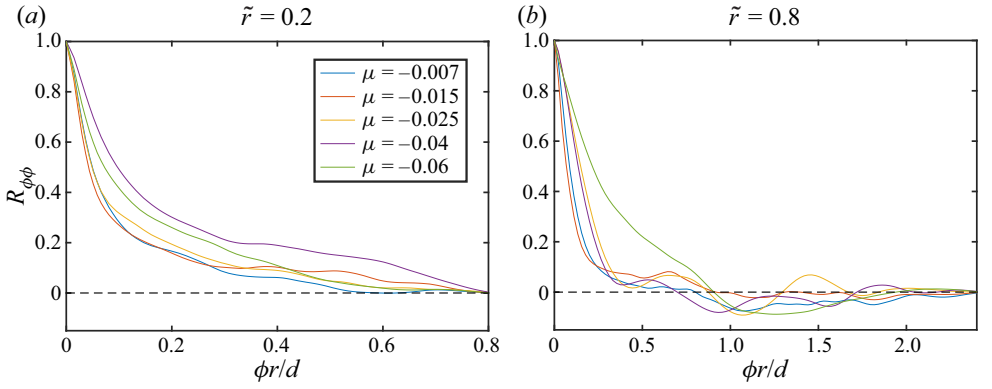


Figure 15. The spatial two-point auto-correlation coefficient of the azimuthal velocity fluctuation for different rotation ratios at the same axial height shown in figures 10–12 for each, at (*a*) $\tilde{r} = 0.2$ and (*b*) $\tilde{r} = 0.8$.

To further study the characteristics of the propagating patterns, especially those observed near the cylinder walls, the spatial two-point auto-correlation coefficient of the azimuthal velocity fluctuation in the azimuthal direction is calculated, where it is defined according to (Dong 2016) as

$$R_{\phi\phi}(r, z, \Delta\phi) = \frac{\langle u'_\phi(r, \phi, z, t) u'_\phi(r, \phi + \Delta\phi, z, t)\rangle_t}{\langle u'^2_\phi(r, \phi, z, t)\rangle_t}, \tag{4.6}$$

with $\Delta\phi$ the azimuthal distance between every two correlated points. Figure 15 depicts the results for two radial positions, one next to the inner wall and the second next to the outer wall. For $\tilde{r} = 0.2$, figure 15(*a*) shows that the auto-correlation function monotonically decreases for all the counter-rotation cases shown in the figure. On the other hand, and for the radial position $\tilde{r} = 0.8$, figure 15(*b*) shows that the auto-correlation function for the different $\mu$ achieves minimums at different $\phi r/d$ values, which indicate the existence of azimuthal structure at this radial position with different sizes depending on the rotation ratio. For $\mu = -0.06$, the minimum is observed for $\phi r/d \approx 1.25$, which is interpreted as the size of the newly observed patterns.

These small-scale turbulent structures are formed in the outer cylinder shear layer and increase the transport in the outer part of the gap and so throughout the entire gap. Obviously, from figure 9(*a*) the contribution of $Nu_\omega^{Turb}$ increases by increasing the counter-rotation; this can explain why the value of the Nusselt number increases for high counter-rotation. But as our measurements are limited to $\mu = -0.06$, it is not possible to know if this increase will continue for higher counter-rotating cases and where the position of the second $\mu_{max}$ will be in the high counter-rotating rates, as theoretically, for very large $\mu$, the flow should stabilize the fluid in the whole gap and the Nusselt number has to decrease to a value near 1.

The first maximum of the Nusselt number that appears in the low counter-rotating regimes is due to centrifugal instability, and this maximum is in agreement with the predicted torque maximum of the enhanced LSC theory predicted by Brauckmann & Eckhardt (2013). The appearance of the second maximum at high counter-rotations is a new finding of this study, and the source of the high transport is connected to the strong turbulent structures inside the outer cylinder shear layer. From the observations of the flow structures, the existence of shear layer instability is assumed, which leads to

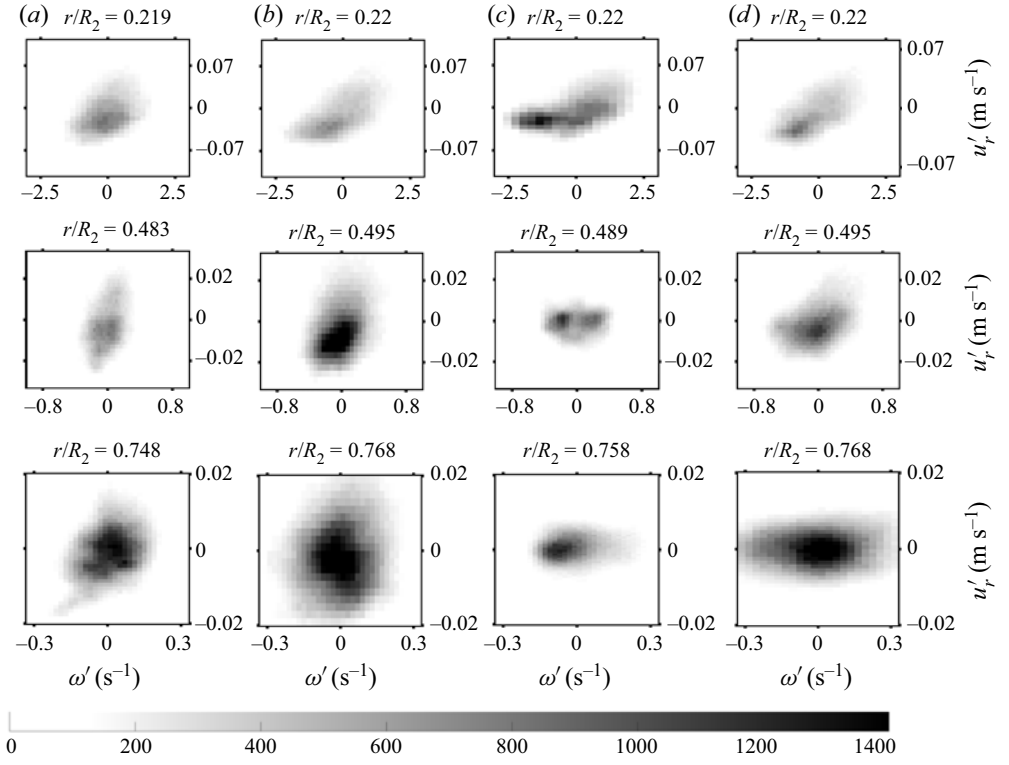


Figure 16. Joint PDFs of radial velocity fluctuations $u_r'$ and angular velocity fluctuations $\omega'$ for radial positions (top row) close to the inner cylinder (figures 10–12, first row), (second row) centre of the gap (figures 10–12, third row) and (bottom row) close to the outer cylinder (figures 10–12, fifth row). Results are shown for the rotation rates (*a*) $\mu = 0$, (*b*) $\mu = -0.0077$, (*c*) $\mu = -0.025$ and (*d*) $\mu = -0.06$, for a shear Reynolds number of $Re_s = 6.1 \times 10^4$.

increases in transport. Figure 8(*b*) shows that as $Re_s$ increase, $\mu_{min}$ approaches more to $\mu_{max}$, in other words, as the shear of the system increases, the shear instability can start earlier to contribute to the angular momentum transport for lower counter-rotating rates, and after that, it is observed how the $Nu_\omega$ starts to increase again. The mechanism by which these patterns are generated is still unclear to us. Tanaka, Kawata & Tsukahara (2018) investigated the existence of modal structures near the outer cylinder for TC flow with $\eta = 0.2$ where they mentioned that, because of the coherent structures on the inner cylinder's unstable side, the velocity disturbance could trigger Tollmien–Schlichting waves at the stable outer cylinder, resulting in these modal structures. It is not clear if the newly observed patterns from the current study are similar or not to these modal structures. Because of this, a future study will concentrate on this aspect and investigate the reason and behaviour of this shear layer instability in more detail at very strong counter-rotation.

For a better understanding of the patterns observed in the space–time plots, the quadrant map of the fluctuating components of $u_r$ and $\omega$ is shown in figure 16. The quadrant analysis is a turbulence data-processing technique, and it has been applied over time in various experimental analyses, mainly in the investigation of turbulent shear flows (Wallace 2016; Hasanuzzaman *et al.* 2020).

The fluctuations of two velocity components are scattered around their mean value and distributed into four quadrants considering their signs. In the current study, the pair of

$(\omega', u_r')$ is represented. The numbering of quadrants is done counterclockwise starting with $Q_1$ for both positive values of $(\omega', u_r')$, $Q_2$ with $\omega' < 0$ and $u_r' > 0$, $Q_3$ with $\omega' < 0$ and $u_r' < 0$, and $Q_4$ with $\omega' > 0$ and $u_r' < 0$. In figure 16 the data are contoured in terms of probability density, so the darkest zones in each plot correspond to the largest concentrations of instantaneous fluctuations for that position.

Figure 16 shows the quadrant map of $(\omega', u_r')$ for different rotation rates at three different radial positions distributed in the inner gap region, middle of the gap and outer region. The velocities used for the current analysis belong to the same experiments used in figures 10–12, with the same axial position and shear Reynolds number. In the inner regions (the figures at the top), the concentration of the distribution of $(\omega', u_r')$ is mostly in $Q_1$ and $Q_3$ for the different rotation rates, so they form an oval-like shape in the diagonal direction, and they are the fingerprints of the patterns observed in the space–time figures that travel outward. In the middle of the gap, the behaviour changes due to the different rotation rates. For $\mu = 0$ and $\mu = -0.0077$, the main concentration is still in $Q_1$ and $Q_3$, but the difference compared with the inner regions is that the value of $(\omega', u_r')$ decreases and the direction of the oval shape is observed to rotate towards the $y$ axis. These observations are still a figure print of the outward patterns, although with lower intensities than those observed in the inner region, in agreement with what is observed in the space–time plots. For $\mu = -0.025$, two highly concentrated black dots appear in the regions $Q_1$ and $Q_2$. The appearance of these two spots in these regions is a sign of the existence of inward and outward patterns, although with very low intensities, as the values of $\omega'$ and $u_r'$ are very low. This can explain why, at this counter-rotation rate, the behaviour changes. This is seen at $\mu = -0.06$, where the same behaviour is observed but with higher values of $\omega'$ and $u_r'$. In the outer regions (the figures in the bottom), for $\mu = 0$, the oval shape of the black spots in $Q_1$ and $Q_3$ still exists, however, with much lower values of $\omega'$ and $u_r'$. But for $\mu = -0.0077$, the main concentration is also in $Q_1$ and $Q_3$, while some black spots appears in $Q_2$ and $Q_4$, where these spots are in agreement with the very light blue spots that appear in figure 10(*b*) at the same radial position, which is a fingerprint of the existence of very weak patterns travelling inward. For higher counter-rotations $\mu = -0.025$ and $\mu = -0.06$, the appearance of the black spots in $Q_2$ and $Q_4$ increases, which further explains the existence of the patterns that travel inward and how the intensity of this pattern increases as the rotation rate of the outer cylinder in the counter direction is increased. Another important observation from the figures related to the outer region of the gap is that where it is seen for $\mu = 0$ and $\mu = -0.0077$, the $\omega'$ $u_r'$ are more distributed along the $y$ axis, which represents the radial velocity with low angular momentum fluctuations. But, for $\mu = -0.025$ and $\mu = -0.06$, different behaviour is observed, where the fluctuating velocities are more distributed along the $x$ axis, which represents the angular momentum fluctuations, with low radial velocity fluctuations. These results can support the conclusion derived from the space–time plots, where it is concluded that the shear layer instability has a high contribution to the angular momentum transport in the high counter-rotating regimes.

## 5. Conclusion

In this paper the flow field for the very wide gap TC flow ($\eta = 0.1$) was investigated for different shear Reynolds number values between 20 000 and $1.31 \times 10^5$, and different rotation rates. The azimuthal and radial velocity components were measured at different cylinder heights using high-speed PIV. The particle images were captured at 200 frames per second, ensuring that the data was time resolved. This study gives the opportunity

to understand the physics of the flow in a very wide gap TC geometry that has rarely been studied before. The flow in this geometry shows some common behaviours compared with the TC flows in different geometries with larger radius ratios and some different behaviours.

The dependence of the flow field on the different rotation ratios was studied first, where it was noted that the radial component is strongly height dependent, while the azimuthal component is weakly dependent. Until today, it was not clear whether a LSC exists in the wide gaps for $\eta < 0.14$ (Eckardt *et al.* 2007), as here the circumferential length of the inner cylinder is smaller than the gap width, especially for high shear Reynolds numbers and turbulent flow. In the current study the existence of the LSC for $\eta = 0.1$ was proven. Although they are not represented as classical TV, their form is strongly elliptical with a high axial wavenumber.

The radial velocity component formed different inflow and outflow regions through the different heights, so they were described as interlaced fingers from inflow and outflow. Also, by decreasing the $\mu$ for higher counter-rotating rates, it was observed that the radial velocity component mostly vanishes near the outer cylinder but still exists with high magnitudes in the inner region. The angular velocity and angular momentum profiles in the bulk were investigated, finding the smallest radial gradient of angular velocity for low counter-rotating rates of $-0.007 < \mu < -0.02$, where $\mu_{max}$ lies in this interval. These findings are in good agreement with those of Ostilla-Monico *et al.* (2014) and Froitzheim *et al.* (2019*a*). Other findings contradict these studies, as it was found in the current study for the newly investigated geometry that the start of the neutral line detachment from the outer cylinder wall did not coincide with $\mu_{max}$ but the detachment started for the lowest counter-rotating rate before reaching $\mu_{max}$. Also, both theoretical predictions of Esser & Grossmann (1996) and Chandrasekhar (1961) were not able to predict the position of the neutral surface, except for very strong counter-rotating rates, in which case our findings agree with Chandrasekhar (1961) prediction. The earliest observed detachment of the neutral line was explained by the high curvature of the system, which allows the outer cylinder to stabilize the flow next to it at very low counter-rotating rates.

The angular momentum transport is quantified from the velocity fields, and the resulting quasi-Nusselt number shows its highest values for the different studied shear Reynolds numbers at the low counter-rotation regions, so $\mu_{max}$ was found for $-0.007 < \mu < -0.012$. The value of $Nu_\omega$ decreases for higher counter-rotation and achieved $\mu_{min}$ and tends to increase again for decreasing $\mu$, where it is expected to achieve a second maximum. The value of the first $\mu_{max}$ shows independence in the shear Reynolds number, while the values of $\mu_{min}$ were shifted toward high counter-rotation rates as the shear Reynolds number decreased.

For further information and in order to understand the $Nu_\omega$ double maxima behaviour with the advantage of a time-resolved measurement, the space–time behaviour of the velocity field at different rotation rates was analysed. For all the counter-rotating cases studied, patterns that travel radially outward through the gap were observed, and the intensity and lifetime of these patterns show a clear dependence on the rotation ratio. When compared with the other studied cases, these patterns appeared to have the highest intensity and longest lifetime for $\mu_{max}$. Another set of patterns was found for the high counter-rotating cases, but in contrast to the previously mentioned patterns, these patterns just appear in the region next to the outer cylinder and propagate inward through the gap. The existence of these inwardly propagating patterns at high counter-rotating rates can explain the increase in angular momentum transport there, where we expect a second maximum for higher counter-rotating rates. It was clear that the first maximum

of $Nu_\omega$ is due to centrifugal instability, and this is explained by the patterns travelling outwards through the gap. The increase of angular momentum transport for even higher counter-rotations was counterintuitive, but from our observations of the flow structures, especially the inward travelling patterns, the existence of a shear layer instability is assumed, which causes the increase in the angular momentum transport.

In order to better understand the behaviour shown in the space–time figures, the fluctuating components of $u_r'$ and $\omega'$ were analysed using the quadrant method, where they showed a good agreement with the space–time plots. They show the existence of inward patterns in the outer region of the gap for high counter-rotating ratios. A conclusion can be derived here: that these patterns are a source of convective terms and, thus, are the reason for the increase in Nusselt number. The figures show that the magnitude of the angular velocity fluctuations increased in the regions near the outer cylinder for high-counter rotating cases. This observation supports our assumption of the existence of a shear layer instability responsible for the increase in angular momentum transport in the high counter-rotating cases.

Only the counter-rotation was studied in this paper. The co-rotation, especially in the centrifugal stable regime, will be the scope of another study as the flow drastically changes and needs different aspects of analysis. Also, we look forward to further analysing our time-resolved data using different methods like dynamic mode decomposition. Our results raise different open questions that we wish to answer in the future, especially about the behaviour of the boundary layers.

**Acknowledgements.** We gratefully acknowledge financial support from DFG EG100/23-1 and EG100/30-1. Also, we would like to thank Stefan Rohark for the technical support.

**Declaration of interests.** The authors report no conflict of interest.

**Author ORCIDs.**
Mohammed Hussein Hamede https://orcid.org/0000-0003-4259-0523.

## References

Andereck, C.D., Liu, S.S. & Swinney, H.L. 1986 Flow regimes in a circular Couette system with independently rotating cylinders. *J. Fluid Mech.* **83**, 155–164.

Brauckmann, H.J. & Eckhardt, B. 2013 Intermittent boundary layers and torque maxima in Taylor–Couette flow. *Phys. Rev.* **87**, 033004.

Brauckmann, H.J., Salewski, M. & Eckhardt, B. 2016 Momentum transport in Taylor–Couette flow with vanishing curvature. *J. Fluid Mech.* **790**, 419–452.

Burin, M.J., Schartman, E. & Ji, H. 2010 Local measurements of turbulent angular momentum transport in circular Couette flow. *Exp. Fluids* **48**, 763–769.

Busse, F.H. 2012 The twins of turbulence research. *Physics* **5**, 4.

Chandrasekhar, S. 1961 *Hydrodynamic and Hydromagnetic Stability*, 1st edn. Clarendon.

Coles, D. 1965 Transition in circular Couette flow. *J. Fluid Mech.* **21**(3), 385–425.

Dong, S. 2016 Turbulent flow between counter-rotating concentric cylinders: a direct numerical simulation study. *J. Fluid Mech.* **615**, 371–399.

Dong, S. & Zheng, X. 2011 Direct numerical simulation of spiral turbulence. *J. Fluid Mech.* **668**, 150–173.

Dubrulle, B., Dauchot, O., Daviaud, F., Longaretti, P.-Y., Richard, D. & Zahn, J.-P. 2005 Stability and turbulent transport in Taylor–Couette flow from analysis of experimental data. *Phys. Fluid* **17**, 118–149.

Eckardt, B., Grossmann, S. & Lohse, D. 2007 Torque scaling in turbulent Taylor–Couette flow between independently rotating cylinders. *J. Fluid Mech.* **581**, 095103.

Esser, A. & Grossmann, S. 1996 Analytical expression for Taylor–Couette stability border. *Phys. Fluids* **8**, 1814–1819.

Ezeta, R., Sacco, F., Bakhuis, D., Huisman, S.G., Ostilla-Mónico, R., Verzicco, R., Sun, C. & Lohse, D. 2020 Double maxima of angular momentum transport in small gap $\eta = 0.91$ Taylor–Couette turbulence. *J. Fluid Mech.* **900**, A23.

Froitzheim, A., Ezeta, R., Huisman, S.G., Merbold, S., Sun, C., Lohse, D. & Egbers, C. 2019*a* Statistics, plumes and azimuthally travelling waves in ultimate Taylor–Couette turbulent vortices. *J. Fluid Mech.* **876**, 733–765.

Froitzheim, A., Merbold, S. & Egbers, C. 2017 Velocity profiles, flow structures and scalings in a wide-gap turbulent Taylor–Couette flow. *J. Fluid Mech.* **831**, 330–357.

Froitzheim, A., Merbold, S., Ostilla-Monico, R. & Egbers, C. 2019*b* Angular momentum transport and flow organization in Taylor–Couette flow at radius ratio of $\eta = 0.357$. *Phys. Rev.* **4**, 084605.

Görtler, H. 1954 On the three-dimensional instability of laminar boundary layers on concave walls. *NACA Tech. Rep.* TM 1375.

Grossmann, S. & Lohse, D. 2000 Scaling in thermal convection: a unifying theory. *J. Fluid Mech.* **407**, 27–56.

Grossmann, S., Lohse, D. & Sun, C. 2016 High-Reynolds number Taylor–Couette turbulence. *Annu. Rev. Fluid Mech.* **80**, 53–80.

Hamede, M.H., Merbold, S. & Egbers, C. 2023 Experimental method for investigating the formation of flow patterns in a very wide gap Taylor–Couette flow ($\eta = 0.1$). *Tech. Mess.* doi:10.1515/teme.2022.0107

Hasanuzzaman, G., Merbold, S., Cuvier, C., Motuz, V., Foucaut, J.-M. & Egbers, C. 2020 Experimental investigation of turbulent boundary layers at high Reynolds number with uniform blowing. Part I: statistics. *J. Turbul.* **21**(3), 129–165.

Huisman, S.G., van Gils, D.P.M., Grossmann, S., Sun, C. & Lohse, D. 2012 Ultimate turbulent Taylor–Couette flow. *Phys. Rev. Lett.* **108**, 024501.

Huisman, S.G., van Gils, R.C.A., Sun, C. & Lohse, D. 2014 Multiple states in highly turbulent Taylor–Couette flow. *Nat. Commun.* **5**, 3820.

Ji, H., Burin, M.J., Schartman, E. & Goodman, J. 2006 Hydrodynamic turbulence cannot transport angular momentum effectively in astrophysical disks. *Nature* **444**, 343–346.

Kawata, T. & Alfredsson, P.H. 2016 Turbulent rotating plane Couette flow: Reynolds and rotation number dependency of flow structure and momentum transport. *Phys. Rev. Fluids* **1**, 034402.

Lathrop, D.P., Fineberg, J. & Swinney, H.S. 1992 Transition to shear-driven turbulence in Couette–Taylor flow. *Phys. Rev.* **46**, 6390–6405.

Lewis, G.S. & Swinney, H.S. 1999 Velocity structure functions, scaling and transitions in high-Reynolds-number Couette–Taylor flow. *Phys. Rev.* **59**, 5457–5467.

Lim, T.T., Chew, Y.T. & Xiao, Q. 1998 A new flow regime in a Taylor–Couette flow. *Phys. Fluids* **10**, 3233.

Merbold, S., Brauckmann, H.J. & Egbers, C. 2013 Torque measurements and numerical determination in deferentially rotating wide gap Taylor–Couette flow. *Phys. Rev.* **87**, 023014.

Merbold, S., Hamede, M.H., Froitzheim, A. & Egbers, C. 2023 Flow regimes in a very wide-gap Taylor–Couette flow with counter-rotating cylinders. *Phil. Trans.* A. doi:10.1098/rsta.2022.0113.

Nordsiek, F., Huisman, S.G., van der Veen, R.C.A., Sun, C., Lathrop, D.P. & Lohse, D. 2015 Azimuthal velocity profiles in Rayleigh-stable Taylor–Couette flow and implied axial angular momentum transport. *J. Fluid Mech.* **774**, 342–362.

Ostilla-Monico, R., Huisman, S.G., Janninik, T.J.G., van Gils, D.P.M., Verzicco, R., Grossmann, S. & Lohse, D. 2014 Optimal Taylor–Couette flow: radius ratio dependence. *J. Fluid Mech.* **747**, 1–29.

Paoletti, M.S. & Lathrop, D.P. 2011 Angular momentum transport in turbulent flow between independently rotating cylinders. *Phys. Rev.* **106**, 024501.

Ravelet, F., Delfos, R. & Westerweel, J. 2010 Influence of global rotation and Reynolds number on the large-scale features of a turbulent Taylor–Couette flow. *Phys. Fluids* **22**(5), 055103.

Razzak, M.A., Khoo, B.C. & Lua, K.B. 2019 Numerical study on wide gap Taylor–Couette flow with flow transition. *Phys. Fluids* **31**, 113606.

Salewski, M. & Eckhardt, B. 2015 Turbulent states in plane Couette flow with rotation. *Phys. Fluids* **27**, 045109.

Saric, W.S. 1994 Görtler vortices. *Annu. Rev. Fluid Mech.* **26**, 379–409.

Synge, J.L. 1938 On the stability of a viscous liquid between rotating coaxial cylinders. *Phys. Fluids* **167**, 250–256.

Tanaka, R., Kawata, T. & Tsukahara, T. 2018 DNS of Taylor–Couette flow between counter-rotating cylinders at small radius ratio. *Intl J. Adv. Engng Sci. Appl. Math.* **10**(2), 159–170.

Taylor, G.I. 1923 Stability of a viscous liquid contained between two rotating cylinders. *Phil. Trans. R. Soc. Lond.* A **223**, 289.

Tokgöz, S., Elsinga, G.E., Delfos, R. & Westerweel, J. 2012 Spatial resolution and dissipation rate estimation in Taylor–Couette flow for tomographic piv. *Exp. Fluids* **53**, 561–583.

VANGILS, D.P.M., HUISMAN, S.G., SUN, C. & LOHSE, D. 2012 Optimal Taylor–Couette turbulence. *J. Fluid Mech.* **706**, 118–149.

VAN DER VEEN, R.C.A., HUISMAN, S.G., MERBOLD, S., HARLANDER, U., EGBERS, C., LOHSE, D. & SUN, C. 2016 Taylor–Couette turbulence at radius ratio: scaling, flow structures and plumes. *J. Fluid Mech.* **799**, 334–351.

WALLACE, J.M. 2016 Quadrant analysis in turbulence research: history and evolution. *Annu. Rev. Fluid Mech.* **58**, 48–131.

WENDT, F. 1933 Turbulente Strömungen zwischen zwei rotierenden koaxialen Zylindern. *Ing.-Arch.* **4**, 577.